SYNTHESIS AND CHARACTERISATION OF INTERGROWTH TUNGSTEN BRONZES AND EVALUATION OF THEIR ELECTROCHEMICAL PERFORMANCE

RYAN DAVID KERR

Synthesis and Characterisation of Intergrowth Tungsten Bronzes and Evaluation of their Electrochemical Performance

SUBMITTED FOR THE DEGREE OF MASTER OF SCIENCE
DURHAM UNIVERSITY, DEPARTMENT OF CHEMISTRY

RYAN DAVID KERR
SEPTEMBER 2020

Abstract

The UK is becoming increasingly reliant on renewable energy sources as a replacement for fossil fuels. There is increasing pressure to reduce the consumption of fossil fuels and, as a result, there is increasing pressure on the energy industry to meet demands for renewable energy. However, this demand cannot be met without the means to store energy during off-peak hours, for use during peak energy consumption hours. Lithium ion batteries provide the solution to this demand, though much work needs to be done to bring battery technology up to the required capacity.

Since their commercialisation in 1991, lithium-ion batteries have become safer and more efficient, partly as a result of the adoption of graphitic anodes, at the expense of electrochemical capacity. In recent years, new energy materials have come forward promising greater capacity to store and provide energy whilst retaining the all-important safety features of intercalation materials. In particular, the work of Griffith et al. has hinted towards safe, reliable and cost-efficient metal oxide anodes with greater electrochemical capacity than the graphitic anodes currently in use across the globe (K. J. Griffith et al., 2018). By selecting the right structural motifs, materials previously thought unsuitable for use as electrodes might provide the solution to the world's demand for safe and storable energy.

This thesis focuses upon the unique interlocking (or 'intergrowth') tungsten bronze (ITB) phase, first reported by Hussain and Kihlborg, for which testing under battery conditions has not yet been conducted (A. Hussain and L. Kihlborg, 1976). $K_{0.13}WO_3$, which is predicted to exhibit an ITB phase, was synthesised and attempts to elucidate its structure via PXRD were made. Galvanostatic discharge-charge data up to an including the third discharge demonstrated that $K_{0.13}WO_3$ has a capacity of 1.60 Li^+/TM on the third discharge, exceeding the capacities of $Nb_{16}W_5O_{47}$ (~1.5 Li^+/TM) and $Nb_{18}W_{16}O_{93}$ (~1.4 Li^+/TM) reported by Griffith et al. at similar rates of discharge. Furthermore, solid-state ^7Li and ^6Li MAS NMR experiments were conducted, suggesting that Li^+ reversibly intercalated into WO_3-like environments in the ITB phase as opposed to the hexagonal sites which were also present.

Abbreviations

ASEI	Artificial Solid-Electrolyte Interface
DMC	Dimethyl Carbonate
EC	Ethylene Carbonate
HTB	Hexagonal Tungsten Bronze
ICSD	Inorganic Cambridge Structural Database (www.psds.ac.uk/icsd)
ITB	Intergrowth /Interlocking Tungsten Bronze
LIB	Lithium-Ion Battery
Li^+/TM	Lithium Ions per Transition Metal (measure of capacity)
MAS	Magic Angle Spinning
NMR	Nuclear Magnetic Resonance
PTFE	Polytetrafluoroethylene
PXRD	Powder X-Ray Diffraction
SEI	Solid-Electrolyte Interface
SSNMR	Solid-State Nuclear Magnetic Resonance
TTB	Tetragonal Tungsten Bronze
XRD	X-Ray Diffraction

Table of Contents

Chapter 1 Introduction and Background

1.1 Current Challenges in Energy Research

Alongside the rapid growth in the world's population in recent decades, owing primarily to social and economic developments worldwide, there has been an associated increase in the global demand for energy. At present, most of this energy is generated from non-renewable sources of fuel (coal, oil, and natural gas), however, these fuels are the main sources of greenhouses gases and other pollutants. Growing concerns over the finite nature of these energy sources and potentially disastrous climate change has led to international efforts to reduce the consumption of fossil fuels in the energy industry. In the last ten years alone, there has been a shift towards renewable sources of energy, including solar, wind and hydroelectric power. This has resulted in record-low levels of the UK's energy being generated from fossil fuels.[1,2]

Despite these improvements, the energy sector faces major challenges when it comes to a total shift towards renewable power. Among these challenges is the reliability of renewable sources - e.g., energy generation from solar and wind power is dependent upon weather conditions, resulting in day-to-day fluctuations and notable reductions in production over the course of a year.[3] One solution to this problem is the use of energy storage devices to stockpile excess energy for a later date. Such devices must have long lifecycles, be made from relatively abundant materials at a low cost, as well as being safe to use and environmentally sustainable.[4] Current storage devices include fuel cells (FC), electrochemical capacitors (EC) and lithium-ion batteries (LIB).[5] Although fuel cells have the highest energy densities (energy per unit volume) of all energy storage devices on average, there are some serious concerns regarding their safety in commercial applications.[6] On the other hand, the high power densities (power per unit volume) of electrochemical capacitors make these devices suitable for periods of operation which demand a high current. The drawback to ECs, however, is their very low energy density, making them less suitable for applications which require significant energy storage. It is these properties of electrochemical capacitors that often results in them being paired with lithium-ion batteries in certain applications, including electric and hybrid-electric vehicles.[7]

Since their commercialisation in 1991, lithium-ion batteries have become one of the most widespread energy storage devices in the world, first

in portable electronic devices and more recently in electric vehicles.[8] The massive growth in the market for LIBs since their commercialisation has been one of the driving factors behind contemporary research into new materials for high-performance electrodes in the hopes of evolving these devices to suit the growing global demand for energy.

1.2 Electrochemistry of Batteries

A battery is a device which consists of one or more electrochemical cells, each of which has several key components: a positive electrode (cathode), a negative electrode (anode), and an electrolyte. The electrolyte is the phase which conducts ions (but does not conduct electrons) and is typically a solution. When the electrodes are immersed in the electrolyte and connected via an external circuit, chemical energy is converted to electrical energy via redox reactions, which are driven by the difference in the electrode potentials of each electrode. During the discharging process a battery acts as a galvanic cell: an oxidative reaction occurs at the anode which drives electrons through the external circuit and generates ions that conduct through the electrolyte. At the same time, a reductive reaction occurs at the cathode, removing electrons from the circuit. A schematic representation of this process is shown in Figure 1.1. These reactions can generally be represented by the following half equations,

$$M \rightarrow M^{n+} + ne^{-} \ , \tag{1.1}$$

$$nM + ne^{-} \rightarrow nM^{-} \ . \tag{1.2}$$

The overall voltage of the battery is related to the free energy of the reactions taking place via the Nernst equation, $\Delta G = -nFE$, where E is the voltage of the battery, F is the Faraday constant, and ΔG is the difference in free energy between the reactions taking place at the anode and the cathode. During the charging process, the battery acts as an electrolytic cell. The flow of electrons (and thus ions) is reversed and the electrochemical reactions are no longer spontaneous, instead driven by the provision of a higher potential from the external power supply.[10] However, it is conventional to refer to the electrodes of a battery by their mode of operation during discharge, hence, the negative electrode is termed the anode, and the positive electrode is termed the cathode.

When an electrochemical reaction takes place at either electrode, a concentration gradient is generated within the electrolyte. Whilst the potential difference of the electrodes drives electrons through the external circuit, the movement of ionic species involved in the electrochemical reactions is governed by diffusion along this concentration gradient. Therefore, the current which flows through the external circuit, I, can be related to the rate of reaction by Faraday's Law,

$$rate = \frac{I}{nF}, \tag{1.3}$$

where n is the number of electrons transferred per mole via the reaction and F is Faraday's constant. From Faraday's Law, two simple observations can be made: (1) when a net current flows, there must be net oxidation at the anode and net reduction at the cathode, and (2) when current stops flowing (for example, if the external circuit is broken), the flow of ions also stops. The rate at which a battery operates is given by its C rate, which is defined by the rate at which it discharges relative to its maximum capacity. A battery operating at a rate of 1 C will fully in discharge in 1 hour. This is the convention used through this report.

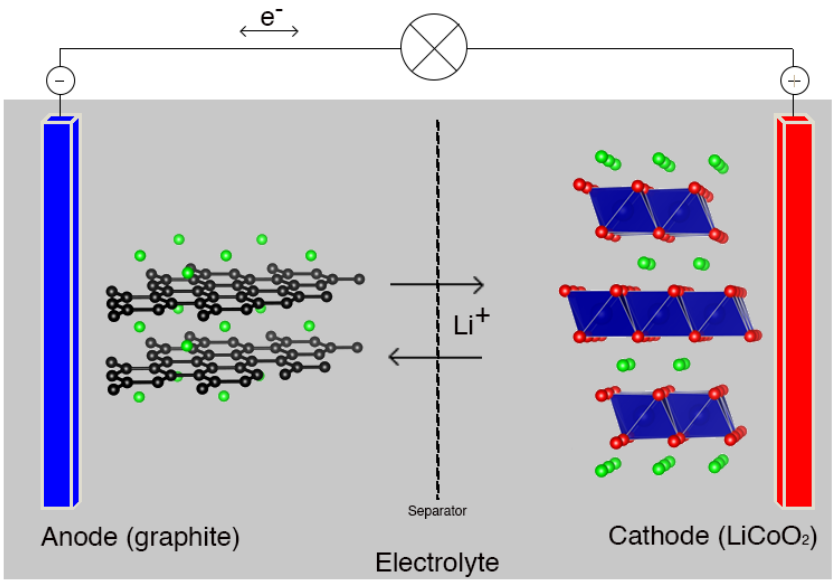

Figure 1.1: Schematic diagram of a lithium-ion battery, showing the direction of the current and the flower of ions during both charge and discharge.

1.3 Lithium-Ion Batteries

Lithium has several properties that make it a suitable candidate for use in energy storage devices. It is the third lightest element, making it ideal for lightweight, portable devices and applications, and has a density of just 0.53 g cm^{-3}. In addition, lithium has the lowest reduction potential of any metal (–3.05 V vs. the standard hydrogen electrode). This gives it a high gravimetric capacity (3860 mA h g^{-1}) surpassed only by that of beryllium.[11] For these reasons, lithium is one of the most promising metals for use in batteries and much work has gone into harnessing its useful properties. However, lithium is a finite resource and there are serious safety concerns regarding its usage.

1.3.1 The Development of Lithium-Ion Batteries

Although the first rechargeable batteries were invented in the 19th century, it was not until the 1970s that the development of rechargeable lithium-ion batteries began.[12] In 1971, researchers at Stanford University reported that some molecules and ions could 'intercalate' into layered tantalum sulphide (TaS_2).[13] Intercalation is the process of reversibly inserting one species between the layers into the crystal structure of another. A battery was subsequently developed with titanium sulphide (TiS_2) as the positive electrode. Chosen for its low weight and electrochemical reversibility, TiS_2 was found to form a single phase when lithium was inserted, which enables lithium to be inserted and removed freely.[14] Lithium perchlorate in dioxolane was used as the electrolyte in this early lithium-ion battery, as $LiClO_4$ would not intercalate into the TiS_2 structure alongside lithium. However, $LiClO_4$ in dioxolane was found to be a potential explosive.[15] Nevertheless, in the late 1970s, Exxon marketed batteries with LiAl anodes and TiS_2 cathodes for use in watches and similar devices.

Very early lithium-ion batteries were affected by the issue of lithium dendrites forming on the anode. These structures would short-circuit the battery, with the sudden discharge generating a significant amount of heat, ultimately igniting the organic electrolyte. Furthermore, dendritic growth on the surface of the anode also leads to fragments of lithium becoming isolated from the electrode. These fragments, sometimes referred to as "dead lithium", are

electrochemically inert but chemically active, accumulating around the electrode and thereby preventing ions from reaching the active electrode.[16]

In 1980, Goodenough et al. discovered that CoO_2 had a layered structure similar to that of TiS_2, and that lithium could be reversibly intercalated between the layers of the structure.[17] With this knowledge, SONY then used $LiCoO_2$ as the cathode in what was to be the first commercially-widespread lithium-ion battery in 1991, where they paired it with a graphitic carbon anode.[17,18] Lithium salts dissolved in ethylene carbonate were used as the electrolyte. In this battery, lithium ions leave the CoO_2 structure during discharge and migrate through the electrolyte to the anode, intercalating into the layered structure of graphite to form LiC_6. The structures and positions of Li^+ in these materials is shown in Figure 1.2. The redox reactions taking place at the anode and cathode, respectively, during discharge are:

$$6\,C_{graphite} + Li^+ + e^- \rightarrow LiC_6\ , \tag{1.4}$$

$$LiCoO_2 \rightarrow Li_{1-x}CoO_2 + x\,Li^+ + x\,e^-\ . \tag{1.5}$$

By intercalating lithium ions into the graphitic anode, the chance of forming lithium dendrites is significantly reduced. This enabled the commercialisation of the C-$LiCoO_2$ battery which has found widespread use in portable electronic devices.

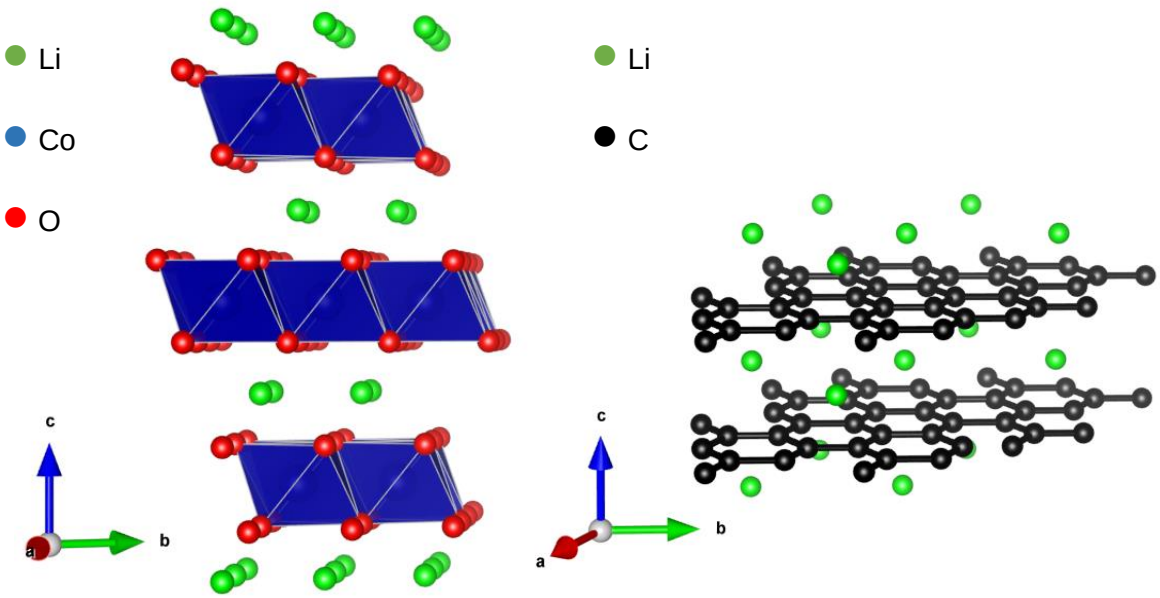

Figure 1.2: Structures of $LiCoO_2$ (left) and LiC_6 (right), displaying their layered structures and the sites of lithiation in each. Images obtained using the VESTA software.

1.3.2 Current Challenges in Lithium-Ion Battery Design

The safety of the lithium-ion battery has been one of the key driving forces behind its development over the last few decades, as discussed above. In particular, the need to reduce or prevent the formation of dendrites on the surface of the anode has seen the implementation of various design features and the use of new materials. However, there are additional factors which must also be taken into account when developing and improving lithium-ion batteries.

The electrolyte of a battery has an associated energy "window" of operation, defined by the difference between its lowest unoccupied molecular orbital (LUMO) and its highest occupied molecular orbital (HOMO). An anode with an electrochemical potential above that of the LUMO will reduce the electrolyte, whilst a cathode with an electrochemical potential below that of the HOMO will oxidise the electrolyte. These unwanted electrochemical reactions can be prevented by (1) choosing electrodes with potentials within the electrolyte window, or (2) including a passivating layer between the electrolyte and the electrode, often referred to as a solid-electrolyte interface (SEI).[19] It is important, however, that the SEI is able to self-heal any fractures that might occur due to changes in the volume of the electrode during operation. For example, the earliest lithium-ion batteries developed by Whittingham et al. used elemental lithium as the anode, owing to its much greater specific energy compared to the now-common graphitic anodes.[20] The electrochemical potential of Li^0 lies above the LUMO of most commonly-used electrolytes, however, its usage is allowed by the passivating SEI layer that is formed after the first charge-discharge cycle. Over the course of a number of charge-discharge cycles, the SEI layer fractures and results in the aforementioned formation of dendrites through the cracks in its surface, and eventually to capacity fading via the formation of dead lithium.[21,22] The risk of SEI deconstruction can be reduced by including an artificial solid-electrolyte interface (ASEI),[23–25] which in turn must follow certain criteria: (1) stable against both the electrode and electrolyte, (2) robust to withstand the formation of dendrites, (3) flexible to accommodate the theoretically infinite volume change that occurs during cycling, and (4) electrically insulating whilst being excellent ionic conductors. These criteria make designing ASEIs extremely difficult, and there is currently considerable research underway into developing new materials to enable to the use of lithium metal electrodes.[26]

Most current lithium-ion batteries utilise an organic liquid electrolyte, in which lithium salts are quite soluble. Typically, these are blends containing a number of carbonates such as ethylene carbonate, diethyl carbonate, dimethyl carbonate, propylene carbonate and ethylmethyl carbonate.[27,28] Of these, ethylene carbonate (EC) is known to form an SEI layer on the surface of graphitic anodes, serving the purpose described above. However, these carbonate-based blends are highly flammable, and the lithium salts dissolved in them can catalytically decompose.[29] Such safety concerns have been the cause of recent research into all-solid-state batteries, utilising solid-state electrolytes in place of organic liquids. Solid electrolytes share similar criteria to ASEIs – primarily, they must have high ionic conductivity, low electrical conductivity, and be electrochemically compatible with both the anode and the cathode.[30] Various types of solid electrolytes exist, including (but not limited to) garnet, perovskite and anti-perovskite structures.[31,32] However, a large range of ionic conductivities has been observed in each family of solid-state electrolytes, owing to the intrinsic link between crystal structure and bulk conductivity, and between density and grain conductivity, such as in the perovskite lithium lanthanum titanate (LLTO), shown in Figure 1.3.[33] In many cases, the introduction of mobile lithium ions into the crystal structure of solid electrolytes may cause distortions which trap or block ions from being transmitted; in other cases, such as in the NASICON-type structure

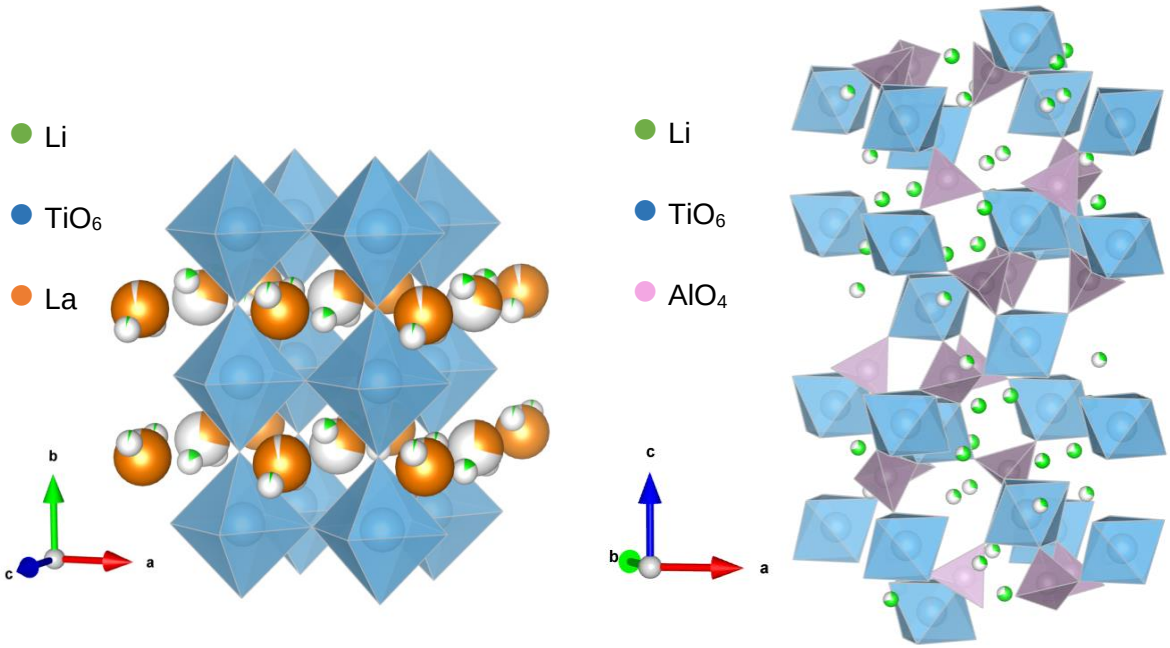

Figure 1.3: Structures of lithium lanthan titanate (left) and NASCION-type $Li_{1+x}Al_xTi_{2-x}(PO_4)_3$ (right). In each, the blue polyhedra represent TiO_6 octahedra and the small green spheres represent Li^+ ions.

$Li_{1+x}Al_xTi_{2-x}(PO_4)_3$, also shown in Figure 1.3, dopants which would otherwise increase ionic conductivity may be readily reduced by the anode.[34,35] Despite these drawbacks, solid electrolytes are an emerging technology of great interest, promising safe, compact and low-weight lithium- and sodium-ion batteries.

As mentioned previously, the chosen electrodes of a lithium-ion battery must also fit certain criteria. The suppression of dendrite formation, discussed above, is not the only concern here; the electrodes must suppress additional side reactions that occur at the electrode-electrolyte interface which, at elevated temperatures, can lead to fire or explosion, known as "thermal runaway".[36] In addition, the chemical stability of the electrodes is of great importance to the longevity of the battery. For example, $LiCoO_2$ suffers from a phase transition which occurs when more than 50% of the intercalated lithium is removed. This transition from the monoclinic to hexagonal phase causes the structure to shrink and, in turn, causes some of the lithium to occupy different sites in the crystal structure. Over time, the cathode is liable to fracture and thus the electrochemical performance deteriorates. Over-discharge in this manner has also been shown to lead to the degradation of the copper current collector at the anode. Electrolysis of the current collector causes copper ions to migrate to the cathode and form dendrites on the surface, eventually leading to internal short circuiting of the battery.[37–39] These unwanted side reactions, which lead to thermal runaway and/or electrochemical degradation of the electrodes, have been shown to be suppressed or reduced entirely by implementing metal oxide coatings via a number of methods.[40]

1.3.3 Advances in Anode Materials

The anode of a lithium-ion battery must be chemically stable against the electrolyte and, ideally, have an electrochemical potential suited to the LUMO of both the electrolyte and the lithium salts dissolved within. Anodes can be grouped into three categories based on their mechanism of operation: conversion, alloying and intercalation reactions.

1.3.3.1 Conversion Reaction Anodes

Most of the materials mentioned so far have been ones in which lithium ions reversibly enter and leave the host system, occupying well-defined sites in the lattice. Conversion reaction anodes work on an entirely different process, in which the ions which diffuse into the material chemically react to form entirely different phases containing lithium. The mechanism of this reaction is illustrated in Figure 1.4.[41] Conversion materials were first discovered in 2000, when reversible electrochemical activity was found in transition metal oxides that were unable to undergo intercalation reactions.[42] The theoretical capacity of these materials ranges from 350 mA h g^{-1} for Cu_2S to as high as 1800 mA h g^{-1} for MnP_4, significantly greater than that of graphite (vide infra).[43] Despite this, conversion-type anodes suffer from major drawbacks, which limits their usefulness in commercial applications. Their discharge-to-charge efficiency is less than that of graphite, meaning that their cyclability is drastically decreased. In addition, the large volume change which accompanies conversion reactions (during both lithiation and delithiation) may lead to failure of the electrode,

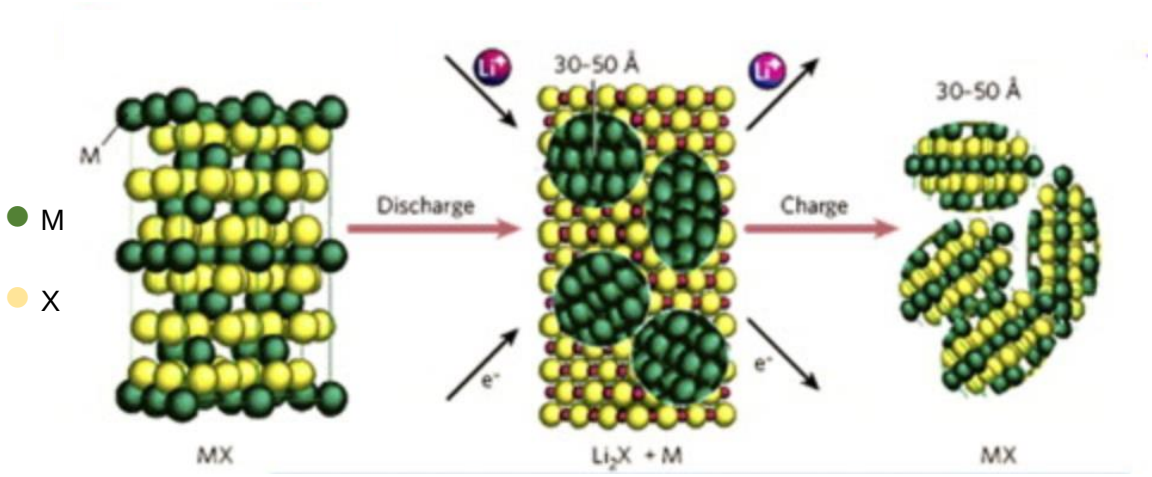

Figure 1.4: Mechanism of a conversion reaction in the context of an anode. Upon discharge, Li^+ enters the host, with composition MX, and forms two separate phases with composition Li_2X and M. When the current is reversed, and the battery is recharged, Li^+ leaves the system and the MX phase is restored.

either by mechanical degradation or electrical isolation. For example, despite the high theoretical capacity of Sn, its structure expands by about 260% upon lithiation.[44]

The latter can be alleviated in several ways, including designing mesoporous materials with high surface areas or hollow structures, allowing room for the structure to expand and contract.[45] In addition, these porous materials can be tailored to improve other properties of the electrode: the walls of the pores in such materials can be made very thin (a few nanometers thick), in order to reduce diffusion path lengths and thereby improve ion conduction, or the material itself can be engineered to incorporate conductive phases, which may eliminate or reduce the amount of conductive carbon that needs to be added to the electrode. Alternatively, conversion-type materials can be combined with carbonaceous nanomaterials.[46] For example, the "peapod-like" structure with MnO particles confined within carbon nanotubes has been demonstrated to exhibit high cyclability and a capacity as high as 1080 mA h g^{-1}.[47]

1.3.3.2 Alloying Reaction Anodes

Another category of anodes are those that operate via alloying reactions, consisting of a group of metallic and semi-metallic elements that can be alloyed with lithium. This group includes the likes of silicon[48], germanium[49] and tin.[50] Alloying reaction materials are known to exhibit extremely high theoretical capacities. For example, an anode in which lithium reversibly alloys with silicon:

$$4.4\ \mathrm{Li^+} + \mathrm{Si} + \mathrm{e^-} \rightarrow \mathrm{Li_{4.4}Si}\ . \qquad (1.6)$$

is known to have a theoretical capacity of 4200 mA h g^{-1}, more than ten times that of graphite. However, as in conversion reactions, anodes which operate via alloying with metals can suffer from extreme volume change during charge and discharge.[51]

Several techniques may be used to mitigate this problem. Firstly, the particles themselves can be reduced in size. The volume of a typical silicon anode changes by up to 400% upon lithium insertion, however, it has been reported that using silicon nanowires as anodes circumvents the issues associated with volume expansion, allowing for good cyclability whilst

retaining the high charge capacity of non-nanostructured silicon anodes.[52,53] Alternatively, carbonaceous buffers may be implemented to allow the active material (e.g., silicon nanoparticles) to expand during lithiation. One such composite was synthesised by encapsulating silicon particles within a carbon nanofibre (CNF), followed by acid treatment to generate nanocavities around the active particles to provide it with space to expand into. This Si-CNF composite had a reversible capacity of 1178 mA h g^{-1} after 60 discharge-charge cycles at various rates.[54]

Another method is the use of ternary alloys, composite materials consisting of three metals chosen for their very special properties. Of these three metals, the first two are electrochemically active and alloy/de-alloy with lithium during operation. The third metal in the alloy is generally used to act as a buffer like the carbonaceous materials noted above, providing some protection against volume expansion. For example, a ternary alloy featured in recent studies is TiSnSb; in this material, both tin and antimony are electrochemically active, whilst titanium was chosen as the buffer material due to its relatively low cost, low toxicity and electrochemical inertia.[55] TiSnSb experiences a +137% change in volume during lithiation whilst providing a reversible capacity of 540 mA h g^{-1} at a rate of 2 C.[56,53] Despite this improved capacity compared to commercially available graphitic electrodes, the volume change exhibited by TiSnSb is still a major factor in determining its applications and potential commercialisation. Much research remains to further reduce it to acceptable levels.

1.3.3.3 Intercalation-based Anodes

Graphite is the representative material for the intercalation reaction family of electrodes. Despite being incompatible with early electrolytes (whereby the electrolyte would be reduced upon lithium insertion), graphite's suppression of dendrite formation has led to its widespread use in portable electronics (vide supra), as well as exhibiting lower reduction potentials than most alternatives. On the other hand, graphitic carbon has a far lower theoretical capacity (372 mA h g^{-1}) compared to the lithium metal electrode (3860 mA h g^{-1}) as only one lithium atom per six carbon atoms can be inserted into the structure.[21,58] Similar carbonaceous materials can be intercalated with lithium to form lithium-carbon intercalation compounds which behave similarly to graphite intercalation compounds electrochemically. Graphitizable carbon (also known as 'soft carbon'), may be intercalated with lithium, however, over repeated discharge-charge cycles the capacity of Li-ion batteries constructed with such anodes fades over time when used with common electrolytes such as propylene carbonate. This is due to the electrolyte itself intercalating into the structure of the crystallites and causing exfoliation, the mechanical process of separating layers during volume expansion. On the other hand, non-graphitizable carbon (also known as 'hard carbon'), which consists of small

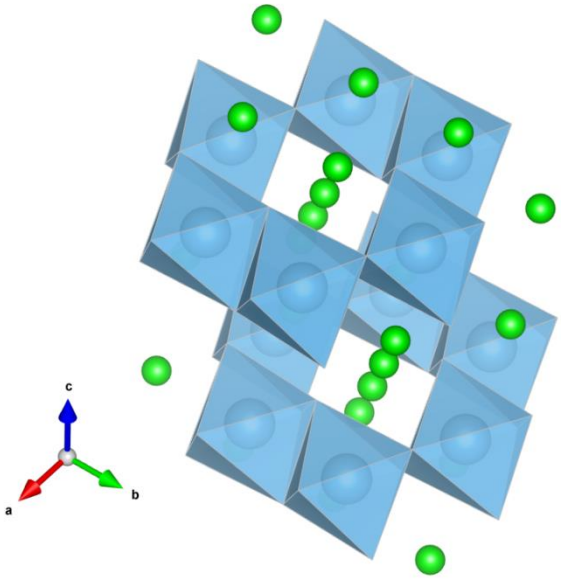

Figure 1.5: Structure of $Li_4Ti_5O_{12}$, clearly showing the channels through which Li^+ ions can diffuse. The blue polyhedra represent TiO_6 octahedra whilst the small green spheres represent Li^+ ions. The oxygen atoms have been omitted for clarity.

crystallites with several randomly orientated layers does not suffer from this capacity fade. Hard carbon is thus referred to as being "highly cyclable".[59]

Lithium titanium oxides (LTO) are non-carbonaceous alternatives for Li-ion battery anodes, first developed in 2008. The most common LTO in commercial use is the spinel $Li_4Ti_5O_{12}$ material, shown in Figure 1.5, with a theoretical capacity of 175 mA h g^{-1}. The structure can accommodate up to three Li^+ upon discharge of the cell (or 0.6 Li^+ per transition metal, TM, present in the unit cell). Although this theoretical capacity is markedly lower than that of graphitic carbon, the volume change which accompanies lithium intercalation into this spinel is just +0.2%. For this reason, the material is referred to as "zero-strain" and has excellent cyclability. In addition, like graphite, the potential of $Li_4Ti_5O_{12}$ is such that it avoids the formation of lithium dendrites. Due to these properties, nanostructured LTOs are suitable in applications where longevity is important, such as in stationary energy storage, and where lower power outputs can be afforded.[60,61]

The intercalation of lithium ions into $Li_4Ti_5O_{12}$, or indeed any intercalation-based anode material, involves three key processes: the diffusion of lithium ions from the electrolyte to the surface of the anode, the charge-transfer reaction that takes place at the surface, and the diffusion of lithium ions into the bulk $Li_4Ti_5O_{12}$.[62] An overall mechanism for this process is displayed in Figure 1.6. The rate of the charge-transfer reaction can be modified by doping small quantities of other elements into the surface of the particles to enhance ionic diffusion.[63] The rate-limiting diffusion of lithium ions

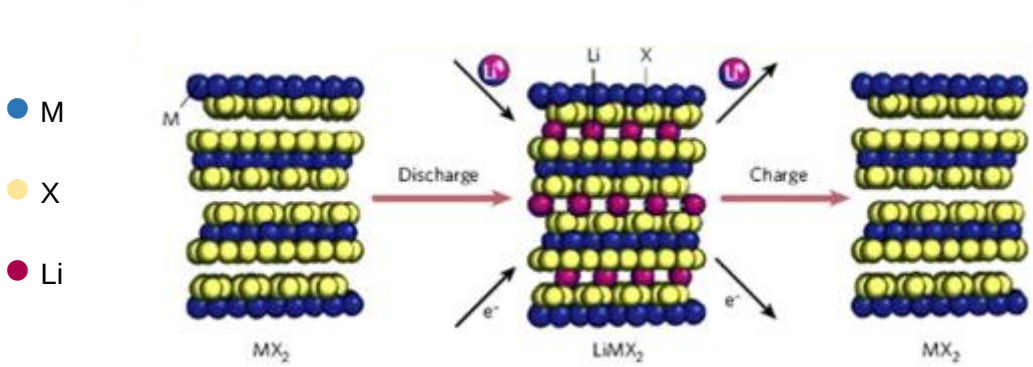

Figure 1.6: Mechanism of an intercalation reaction in the context of an anode. Upon discharge, Li^+ enters the space between layers in host structure, which has a composition MX_2, forming a stucture with the composition $LiMX_2$. When the battery is recharged, Li^+ exits the host structure and its composition becomes MX_2 again. Image adapted under the Creative Commons license from H. Yoo et al., Mater. Today, 2014, 17, 110–121.

may be enhanced by designing nanoscale particles using a variety of synthetic methods, including sol-gel synthesis and molten salt methods.[64–66] Due to their small size and high surface area, the contact between the surface of $Li_4Ti_5O_{12}$ and the chosen electrolyte is maximised whilst the diffusion pathway is reduced, both of which contribute to improved capacity at high rates of charge or discharge. However, reducing particle sizes to the nanoscale does not come without its downsides. The synthesis of such particles is often time-consuming and resource-intensive, resulting in low yields and considerable chemical waste.[67] In addition, while the capacity of the particles may be increased, they may also be vulnerable to decomposition by the catalyst[68] capacity fading[69] and undesirable structural changes.[70]

1.3.4 Niobium Tungsten Oxides

In recent years, the costly downsides to nanoscale synthesis of anode materials has resulted in a drive to find alternative methods of enhancing discharge capacity. One such alternative was proposed by Griffith et al. in July 2018, ultimately forming the basis of this report.[71] They demonstrate that by choosing the appropriate crystal structure the normal constraints of particle size and porosity need not be fulfilled; instead, they synthesised compounds on the microscale which outperformed nanoscale LTOs under similar conditions. Their paper follows an earlier publication concerning the high-rate intercalation of Li into micrometer-sized particles of Nb_2O_5 and Nb_2O_5 in the T and TT phases (shown in Figure 1.7), in which they identified structural motifs that favoured Li diffusion.[72,73] The ‘room-and-pillar’ structure of these low-

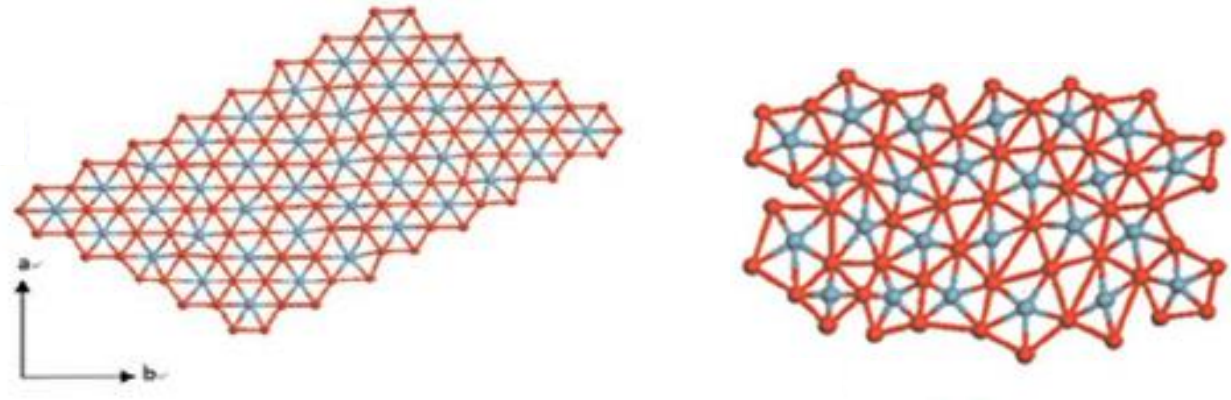

Figure 1.7: Structure of TT-Nb_2O_5 (left) and T-Nb_2O_5 (right), viewed along the c-axis. The niobium atoms are shown in blue, whilst the oxygen atoms are shown in red. Adapted from E. Tsang et al., Nano Rev., 2012, 3, 17631. Copyright 2012, Co-Action Publishing.

temperature Nb_2O_5 polymorphs allows lithium ions to intercalate into the channels (or 'rooms') formed by NbO_6/NbO_7 polyhedra, which link together to form 'pillars'. These channels are supported by bridging oxygen atoms, allowing them to remain open even under the influence of intercalated ions. This allows for high ionic mobility within the structure. Based on this room-and-pillar motif, they synthesised two different niobium tungsten oxides: $Nb_{16}W_5O_{55}$, which has a "block" or "shear"-type structure, and $Nb_{18}W_{16}O_{93}$, which has a 'bronze-like' structure.[74]

1.3.4.1 *"*Shear-type*"* $Nb_{16}W_5O_{55}$

$Nb_{16}W_5O_{55}$ is composed of corner sharing NbO_6 octahedra arranged similarly to ReO_3, forming blocks that are five octahedra wide, four octahedra long and infinite in the third dimension, as illustrated in Figure 1.8. The shape of these blocks is denoted [n x m], where n is the width of the block in octahedra and m is the length. At the edge of these blocks are crystallographic shear planes, in which the adjacent blocks are offset in the third dimension, hence the label "shear-type". It is a metastable compound below about 1090 °C and is known to disproportionate to Nb_2WO_8 and $Nb_{14}W_3O_{44}$ upon cooling.[75,76] Its powder is pale yellow-green in colour.

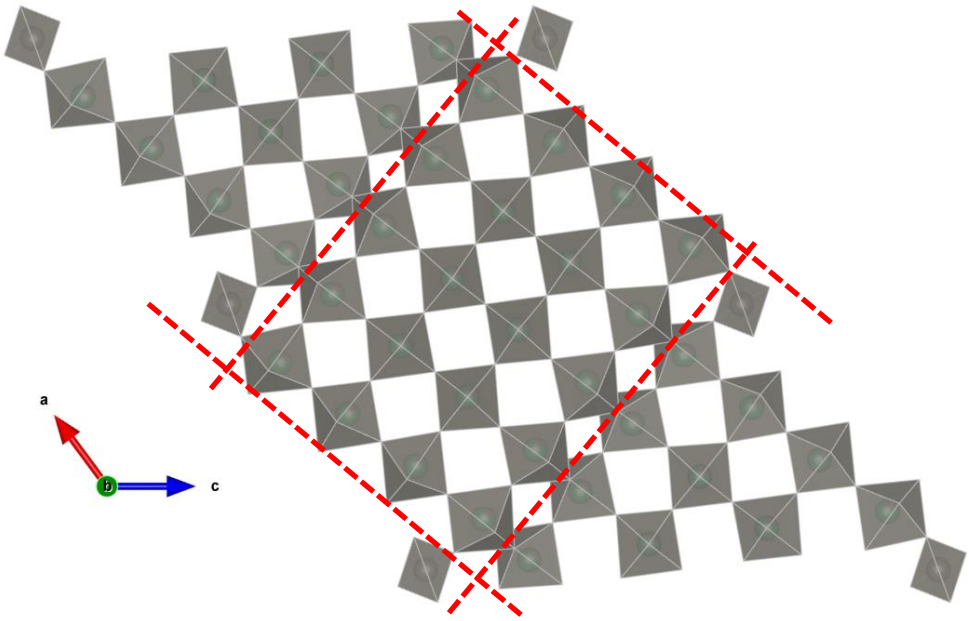

Figure 1.8: The unit **cell of "shear"**-type $Nb_{16}W_5O_{55}$, viewed along the b-axis. The grey polyehedra represent NbO_6 and WO_6 octahedra. The oxygen atoms have been omitted for clarity. The crystallographic shear plans are illustrated as red dashed lines.

The description of $Nb_{16}W_5O_{55}$ given above, however, is a relatively simplistic one. The structure of this material is not homogenous; although initial X-ray diffraction measurements indicated a single phase, high-resolution electron microscopy (HREM) revealed the presence of so-called "Wadsley defects", the ordered intergrowth of one niobium tungsten oxide into the structure of another. These defects manifest as fringes in the HREM images, caused by the insertion of blocks which are not [5 x 4] in dimension, as exemplified in Figure 1.9. Importantly, the presence of these defects can be controlled by long synthesis times, however, their total removal in a gram-scale sample of $Nb_{16}W_5O_{55}$ is believed to be impossible. After 768 hours of high-temperature annealing, Allpress and Roth were able to identify individual particles that contained only a single phase (i.e., zero Wadlsey defects), but these particles were not representative of the entire sample. This is attributed to the very small differences in free energy between adjacent phases, allowing [5 x 4], [4 x 5] and [6 x 5] blocks to readily interconvert between one another at high temperatures.[77]

When tapped density (the maximum density of the powdered material) is considered, the volumetric charge density of $Nb_{16}W_5O_{55}$ was reported to be 548 A h l^{-1} at a discharge rate of 1 C, compared to 103 A h l^{-1} for graphite (particle size: 6 µm). In addition, Griffith et al. found that $Nb_{16}W_5O_{55}$ performed well at high rates of discharge, with a gravimetric capacity of 150 mA h g^{-1} at 20 C.[71] This is significantly greater than that of $Li_4Ti_5O_{12}$ (90 mA h g^{-1} at 20 C).

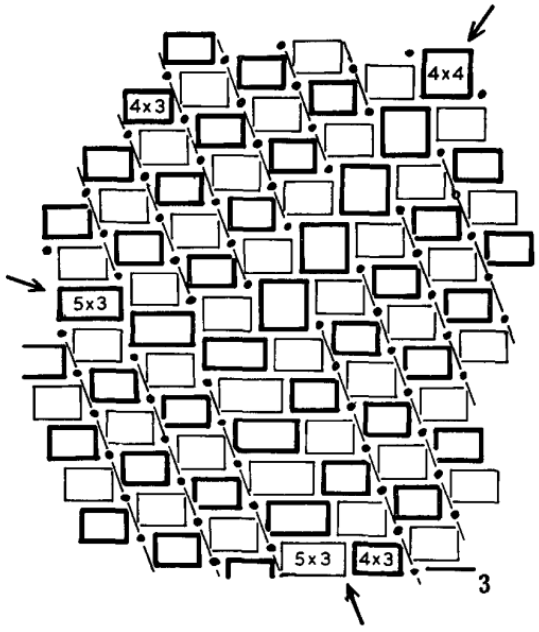

Figure 1.9: Illustration of Wadsley defects in shear-type $Nb_xW_yO_z$ structures. The arrows represent crystallographic shear plans formed by converging [5 x 3] and [4 x 3] defects. Adapted from A. Hussain and L. Kihlborg, Acta Crystallogr. Sect. A, 1976, 32, 551–557.

Furthermore, the material retained 95% of its gravimetric capacity after 1000 cycles, showing excellent cyclability.

1.3.4.2 *"*Bronze-like*"* $Nb_{18}W_{16}O_{93}$

$Nb_{18}W_{16}O_{93}$ has an orthorhombic unit cell with the superstructure of a classic tetragonal tungsten bronze, illustrated in Figure 1.10. This structure results from the partial filling of pentagonal tunnels with metal oxide chains as well as the distorted octahedra of the tetragonal tungsten bronze. Unlike in $Nb_{16}W_5O_{55}$, this material was not found to contain Wadsley defects. In a powdered form, it is described as off-white in colour.

The volumetric charge density of $Nb_{18}W_{16}O_{93}$ was calculated to be 496 mA h l^{-1}, slightly lower than that of $Nb_{16}W_5O_{55}$, owing to its higher molar mass. Its gravimetric capacity at higher rates of discharge was similar to that of $Nb_{16}W_5O_{55}$ and, like the shear-type material, demonstrated excellent cyclability over hundreds of discharge-charge cycles. When testing at higher rates (up to 100 C), Griffith et al. determined that the capacity was primarily limited by lithium metal plating/stripping and lithium ion desolvation rather than by the metal oxide anodes themselves.[71]

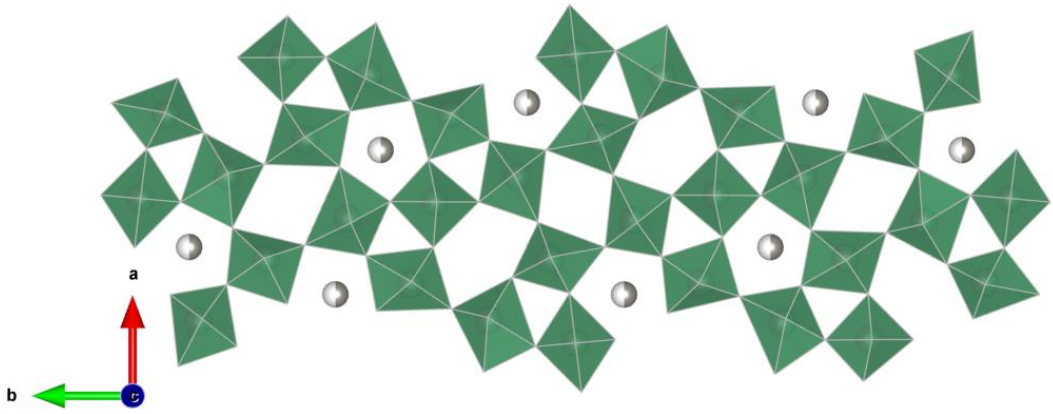

Figure 1.10: Unit cell of $Nb_{18}W_{16}O_{93}$, viewed along the c-axis. The green polyhedra represent NbO_6 octahedra, whilst the white/grey spheres represent the pentagonal sites partially occupied by tungsten atoms.

1.3.4.3 Structural Considerations

Griffith et al. proved, by a variety of methods designed to probe the diffusion of lithium ions both in and out of the two metal oxides detailed above, that the 'impressive' performance of these materials can be directly linked to their structures.[71] More specifically, the crystallographic shear planes in the shear-type $Nb_{16}W_5O_{55}$ and the twisted octahedra linked to pentagonal columns in "bronze-like" $Nb_{18}W_{16}O_{93}$ decrease the structural degrees of freedom.

Both structures can be related to ReO_3 and WO_3, the latter of which being one of the reagents used to prepare samples of both $Nb_{16}W_5O_{55}$ and $Nb_{18}W_{16}O_{93}$. By inspecting these structures, one might assume (at first glance) that ReO_3 and WO_3 are suitable materials for lithium ion storage. However, this is not the case, as their open and flexible framework is known to undergo a structural phase transition upon lithiation.[78] The frustrated polyhedral networks present in $Nb_{16}W_5O_{55}$ and $Nb_{18}W_{16}O_{93}$ do not undergo these transitions upon lithiation, owing to the reduced degrees of freedom afforded by the structural motifs mentioned above. These motifs effectively stabilise the structure and prevent local distortions from causing long-range rearrangements of the framework.

In addition, calculations on the $Nb_{16}W_5O_{55}$ system suggested lithium ions were able to migrate between the twelve adjacent and parallel channels in each [5 x 4] subunit. The ability to 'hop' between channels means that $Nb_{16}W_5O_{55}$ is not susceptible to defects which would otherwise block channels and prevent intercalation, as seen in similar one-dimensional ion conductors such as $LiFePO_4$, a common iron phosphate cathode.[79] Similarly, $Nb_{18}W_{16}O_{93}$ was shown to have a two-dimensional diffusion network in its structure, allowing for ions to migrate between channels running along the c-axis. These observations hold true for niobium tungsten oxides with similar structures and different stoichiometries, although many other non-stoichiometric phases have been found to be unstable at low temperatures and are therefore not suitable for these applications.

1.4 Tungsten Bronzes

Tungsten bronze structures contain one-dimensional channels which run along the c-axis.[80,81] Due to these channels, they are of interest in intercalation chemistry; many tungsten bronzes have demonstrated their ability to accommodate mobile H^+ and Li^+ cations in their structures.[82–84] There are various types of tungsten bronzes, named according to their structures: hexagonal tungsten bronzes (HTBs), tetragonal tungsten bronzes (TTBs), and cubic tungsten bronzes (CTBs), the latter of which will not be expanded upon here. In addition, hexagonal and tetragonal phases have been shown to coexist in what is known as an intergrowth tungsten bronze (ITB), or sometimes as an interphase tungsten bronze.

1.4.1 Hexagonal Tungsten Bronze (HTB)

Most tungsten bronzes with the formula A_xWO_3 exist in the hexagonal phase.[85] The structure of HTBs consist of distorted corner-sharing WO_3 octahedra forming hexagonal tunnels along the c-axis, which the A-site cations occupy. Large cations such as K^+, Rb^+ and Cs^+ can stabilise the structure if they occupy more than half of the A-sites. The unit cell of a hexagonal tungsten bronze is illustrated in Figure 1.11.

The hexagonal tunnels play an important part in the electrochemical behaviour of materials with the HTB structure, and as a result there are many

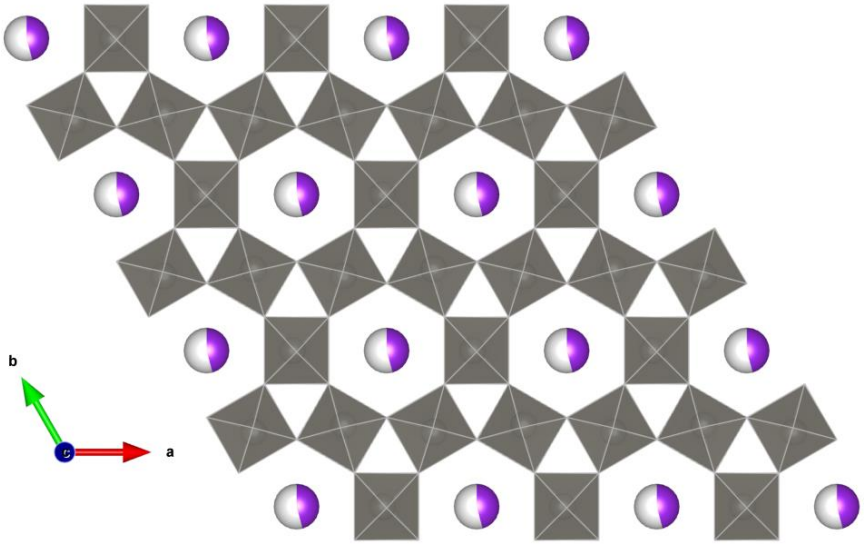

Figure 1.11: Unit cell of the hexagonal phase of $K_{0.3}WO_3$, viewed along the c-axis, with the hexagonal channels clearly shown. The grey polyhedra represent WO_6 octahedra, and the white-purple spheres represent sites partially occupied by K^+ ions.

reports regarding the intercalation of lithium into such materials.[86] However, as mentioned above, the HTB structure often arises from larger cations occupying the cavities within the hexagonal tunnels; cations with smaller ionic radii tend to form pyrochlore phases from the same host structures.[87] The occupancy of the A-sites also affects the phase formed: for a structure $A_xMO_{3+x/2}$, hexagonal phases tend to be formed when $x < 0.33$ – i.e., when up to one third of the A-sites are occupied.[88]

1.4.2 Tetragonal Tungsten Bronze (TTB)

Metal oxides with the TTB structure are based on an array of corner-sharing MO_6 octahedra in the ab-plane that stack along the c-axis to form pentagonal, quadrangular and triangular tunnels, as shown in Figure 1.10 (vide supra).[89] This framework itself is not charge-neutral unless the metal, M, is in the +6 oxidation state, however, the cavities within these tunnels may be occupied by alkali and alkaline earth metal cations to form TTB structures, with the metals in the +5 and +4 oxidation states respectively. In general, the pentagonal cavity (A3-site) in a cross-section of a TTB structure is fully occupied, the quadrangular cavity (A2-site) is half-filed, and the triangular cavity (A1-site) is usually vacant. This generalisation does not preclude the possibility of finding fully occupied TTB structures; such structures have been reported, such as $Pb_2KTa_5O_{15}$ and $Sr_2NaNb_5O_{15}$.[90,91]

1.4.3 Intergrowth Tungsten Bronze (ITB)

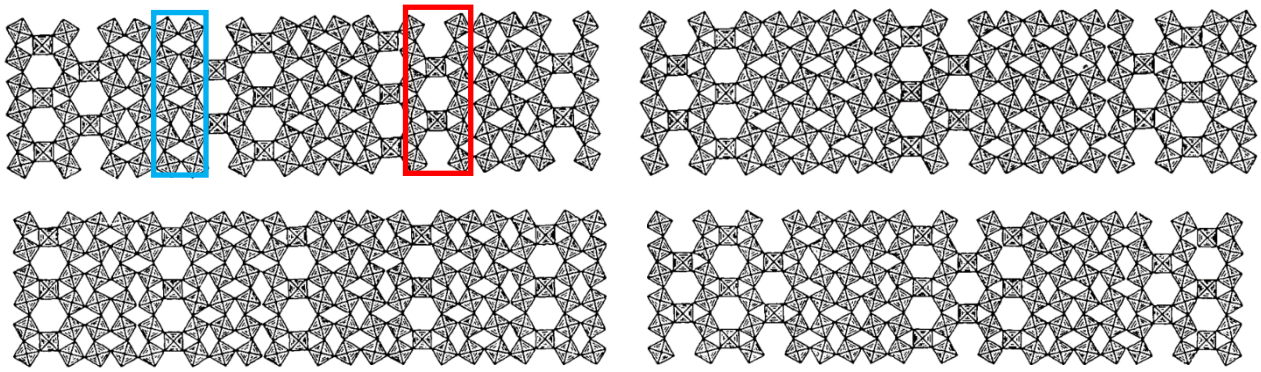

Figure 1.12: Some of the idealised structures of intergrowth tungsten bronzes proposed by Hussain and Kihlborg, showing its fringe-like structure. An ReO_3-type slab is highlighted with a blue box, whilst a HTB-type slab is highlighted with a red box. Adapted from A. Hussain and L. Kihlborg, Acta Crystallogr. Sect. A, 1976, 32, 551–557.

The three main tungsten bronze phases are the hexagonal, tetragonal and cubic phases, however, an additional, unique phase exists for structures with the formula A_xWO_3, where A = K, Rb, Cs. As mentioned above, these cations typically form hexagonal phases at low concentrations of A (i.e., when $x < 0.33$). This additional phase was reported by Hussain and Kihlborg in 1976, where it is referred to as the 'intergrowth tungsten bronze' (ITB) phase.[92] Between $x = 0.01$ and $x = 0.13$, the powders synthesised from heating a mixture of WO_3, WO_2 and A_2WO_4 contained large black crystals in a mass of fine yellow-white powder. The abundance of these black crystals increased with x. Between $x = 0.10$ and $x = 0.13$, these crystals were in coexistence with a hexagonal phase, and the crystals were not found beyond $x = 0.13$, where the powder was singularly in the HTB phase. It was reported that these crystals were not affected by strong alkaline solutions, nor were they affected by acidic solutions.

Hussain and Kihlborg conducted high-resolution electron microscopy (HREM) studies on the black crystals they had synthesised, and by combining these images with X-ray diffraction (XRD) analysis they were able to resolve the structure.[92] The phase can be described as an intergrowth of slabs with HTB structure and slabs with a ReO_3-/WO_3-type structure, in which the corner-sharing WO_6 octahedra were tilted are about 15°. These components alternate in a periodic manner, however, from the first HREM images it was apparent that the widths of the HTB and ReO_3-type slabs varied, as identified by the anomalous widths of the fringes observed in the images. This bears

striking resemblance to the Wadsley defect fringes observed in the $Nb_{16}W_5O_{55}$ shear structure reported by Griffith et al. (vide supra)[71]; indeed, Hussain and Kihlborg noted that most crystals studied via X-ray diffraction gave complex patterns due to two or more lattices with the same b and c cell parameters but different lengths on the a-axis (i.e., slabs of differing width to their neighbours).[92] Nevertheless, they were able to provide a reliable XRD analysis from some of the crystals synthesised. Furthermore, they determined that the width of the HTB slabs was related to the concentration of A in the synthesis. Some of the structures observed are illustrated in Figure 1.12. So far, no electrochemical behaviour has been reported for the intergrowth tungsten bronzes synthesised by Hussain and Kihlborg.

1.5 Research Aims

Lithium-ion batteries have played a pivotal role in the world we live in since their inception in the 1990s. Despite previous safety concerns, ever-increasing research into the components of these batteries have led to life-changing advancements over the last thirty years. The graphite anode continues to be the number one choice for many applications; however, various alternative anode materials have shown that there is great potential for improvement on many key aspects of this component. Conversion-based and alloying-based anodes such as MnP_4 or the ternary alloy TiSnSb have shown that the gravimetric capacity of graphite (372 mA h g^{-1}) is far from the upper limit of contemporary anode materials. On the other hand, the research of Griffith et al. shows that the time-intensive and costly techniques used to prepare intercalation-based materials with higher theoretical capacities than that of graphite can be substituted by choosing materials with an appropriate crystal structure.[71]

The initial portion of this research is based on the report by Griffith et al., wherein the effects of varying experimental conditions on the structures of $Nb_{16}W_5O_{55}$ ("shear"-type niobium tungsten oxide) and $Nb_{6.7}W_{10.3}O_{47}$ ('bronze-like' niobium tungsten oxide, similar in structure to $Nb_{18}W_{16}O_{93}$) will be studied. Following this, the synthesis, characterisation and electrochemical behaviour of a series of potassium tungsten bronzes (K_xWO_3, $0.05 < x < 0.40$) has been studied in order to investigate the intergrowth tungsten bronze (ITB) phase reported by Hussain and Kihlborg.[92] All materials synthesised were characterised using powder X-ray diffraction (PXRD) to determine the phase purity of the sample and, where possible, elucidate the crystal structure and cell parameters. Phase-pure samples, within a margin of error appropriate for structures where Wadsley defect fringes (or similarly structural anomalies) may exist, were then be to create self-supporting thin films. These thin films served as the anode in a cell containing lithium metal, and used to conducted galvanostatic measurements to investigate the lithiation and de-lithiation of the active material. ^6Li and ^7Li MAS solid-state nuclear magnetic resonance (SSNMR) was then used to study the intercalation behaviour of the active material.

Chapter 2 Experimental Techniques

2.1 X-ray Diffraction

2.1.1 Principles of X-ray Diffraction[93,94]

X-ray diffraction can be understood by comparison to the principles of optical diffraction. Consider passing visible light through an optical grating, a piece of glass scored with parallel lines which are separated by a distance comparable to the wavelength of light. The lines of the optical grating can be considered a secondary point source of light which re-radiates light in all directions. Light from one secondary source can interfere either constructively or destructively with light from all other sources, with the mode of interference being governed by the wavelength of the light, λ, and the separation of the lights of the grating. Due to the vast number of secondary sources in the optical grating, the measured diffraction pattern exhibits intense and regularly-spaced bands of light where the diffracted beams are in-phase.

X-rays, with a wavelength of ~1 Å, are diffracted by crystalline structures, in which the interatomic distances are comparable in magnitude (but still somewhat larger than) the wavelength. The highly periodic nature of crystalline structures enables them to function like a diffraction grating for X-rays, with the regular unit cells acting as the secondary point sources. However, an important distinction to make is that, in either case, the incident radiation is not reflected by the diffraction medium. It is instead scattered as a result of its interaction with the atoms' electrons.

The description above is based on the assumption that the sample consists of a single two-dimensional grid of atoms. Although crystals are three-dimensional arrays, the Bragg approach to diffraction considers them as a set of two-dimensional planes which both reflect and transmit radiation. Figure 2.1 illustrates how this approach leads to Bragg's Law,

$$2d \sin\theta = n\lambda \,, \tag{2.1}$$

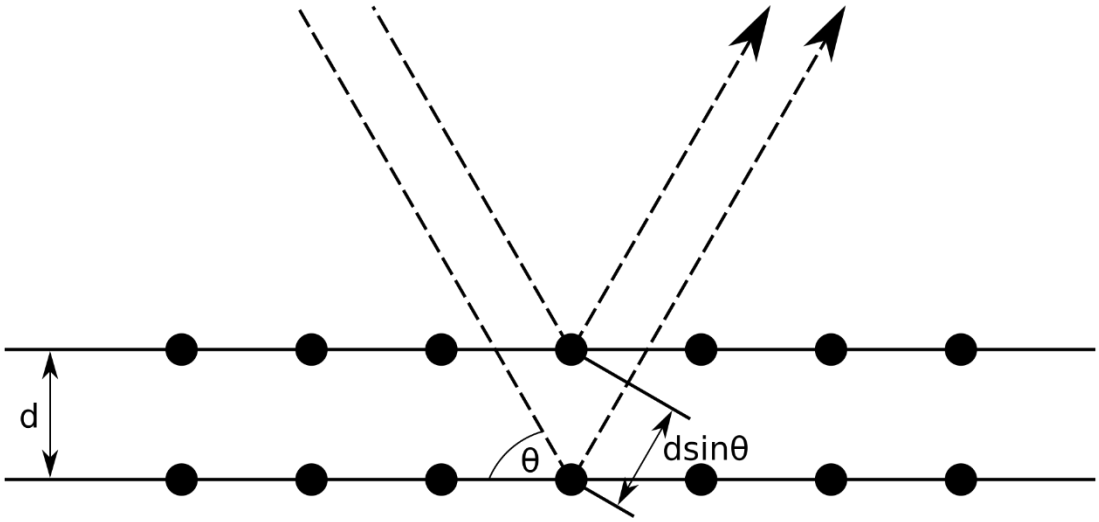

Figure **2.1: Derivation of Bragg's Law, which** treatments a three-dimensional array of atoms as a set of adjacent semi-transparent planes.

where d is the separation between adjacent planes, θ is the angle of the incident X-ray beam, n is an integer and λ is the wavelength of the X-rays. Figure 2.1 shows two incident X-ray beams being scattered by adjacent planes, A and B, which are separated by distance d. For their reflections to be in-phase, the additional distance that beam 2 must travel must be equal to a integer multiple of the wavelength (n = 1, 2, 3…). Since λ is fixed in an X-ray diffraction experiment, and d is a parameter fixed by the sample itself, solutions to Bragg's Law are found by varying θ. For angles where the scattered X-rays are not in phase, destructive interference occurs. For a real crystal, this results in total cancellation of the scattered beams outside a very small range of angles centred around the Bragg angle for any given plane.

In the diffraction experiment, X-rays are generated by striking a metal target, in this case Cu, with a beam of accelerated electrons. This causes the ionisation of the metal and, subsequently, an electron from the core shell is emitted. It is replaced by an electron from a higher energy orbital, simultaneously emitting X-ray radiation to account for the change in energy.

2.1.2 Powder X-ray Diffraction

In an ideal, finely-powdered sample, all crysallites are randomly arranged in all possible orientations. Some of these planes must be orientated at the Bragg angle with respect to the incident radiation, and therefore constructive interference occurs for these. When X-ray radiation is incident upon the

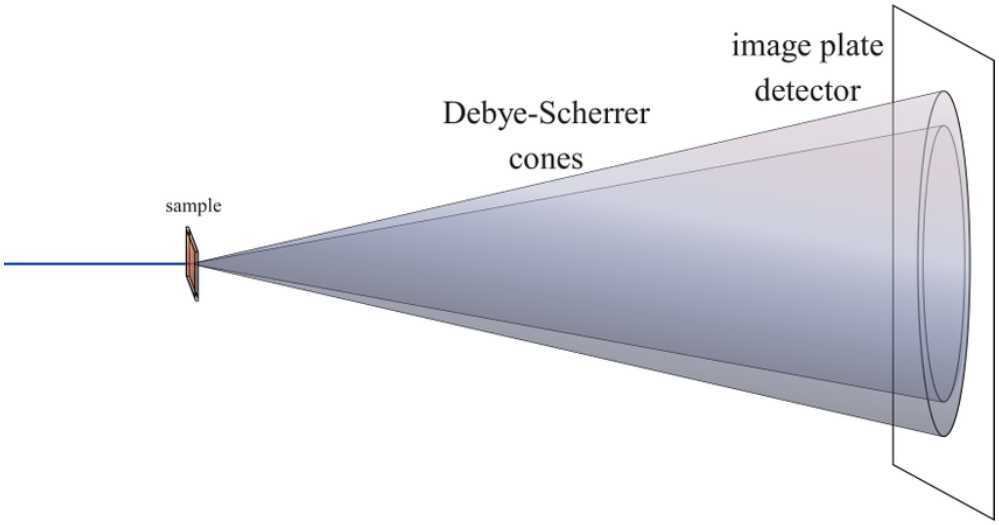

Figure 2.2: Debye-Scherrer cones obtained from the diffraction of a monochromatic X-ray beam by a powdered, crystalline material. Adapted from J. Kieffer and J. Wright, Powder Diffr.,, DOI:10.1017/S0885715613000924.

sample at a given Bragg angle, the diffracted beams form a Debye-Scherrer cone of radiation unique to the targeted set of planes due to the angular orientation of the planes around the direction of the incident beam. This is illustrated in Figure 2.2.[95]

In powder X-ray diffraction (PXRD) experiments, the angle of incidence is varied through a range of angles whilst the sample is rotated. The detector scans through the reflected cones at each step and the intensity of the cones is plotted against 2θ.

2.1.3 Experimental Procedure

Samples were ground into fine powders using an agate mortar and pestle. A glass slide was prepared by applying a moderate amount of grease. The sample was applied using a 250 micron sieve to ensure the powder was uniformly distributed across the slide. Diffraction patterns were recorded on a Bruker d8 diffractometer using Cu $K_{\alpha 1}$ radiation (λ = 1.54056 Å). Scans were taken over a 2θ range of 10-60°, unless specified otherwise, incremented in 0.02° steps.

2.1.4 Rietveld Refinements

The Rietveld method is used to fit an experimentally-obtained diffraction pattern to a theoretical diffraction pattern. The theoretical diffraction pattern is

usually obtained from the Inorganic Crystal Structural Database (ICSD)[96] as a crystallographic information file (.cif file). It may also be constructed from a table of atomic positions in molecular modelling and visualisation software such as VESTA or CrystalMaker. This process is used primarily to determine the phase composition of a powdered sample (the phases present and their relative contributions to the overall diffraction pattern). Structural information such as bond angles, bond lengths and unit cell dimensions can be obtained from the results of a Rietveld refinement.

During a Rietveld refinement, a range of parameters are varied to minimise the residual, S_Y, of the calculated (Y_{ci}) and observed (Y_{oi}) diffraction patterns using a least squares approach:

$$S_Y = \sum_i \frac{1}{Y_{oi}} (Y_{oi} - Y_{ci})^2 \ . \qquad (2.2)$$

The parameters refined include the detector zero point, lattice parameters, atomic coordinates and thermal parameters, the background and profile coefficients (which determine the Lorentzian and Gaussian contributions to the shape of the diffraction peaks). The accuracy of a Rietveld refinement is determined by either the χ^2 value or the weighted R-factor, wRp. An acceptable fit is obtained when either $\chi^2 \approx 1$ or wRp < 20%. In this report, all Rietveld refinements were carried out using the General Structural Analysis System-II (GSAS-II).[97]

2.2 Galvanostatic Measurements

2.2.1 Electrode Preparation

Self-supporting film electrodes were prepared using polytetrafluroethylene (PTFE) as a binder and superconductive carbon black as a conductive additive. Alongside the active material, these components were dry mixed and ground by hand in an agate pestle and mortar in a weight ratio of 70:18:12 (active material, conductive additive and binder, respectively) until the mixture plasticised. Thin, self-supporting discs were cut out and adhered to copper mesh, then dried under vacuum at 100 °C.

2.2.2 Electrochemical Cell Construction

Swagelok™ cells were used for the electrochemical testing of all electrodes prepared in this report. These contain two plungers, one at either end of the cell, with which the anode, cathode and separator discs can be pressed and locked together by hand, as illustrated in Figure 2.3. All components of the cell, except for the lithium metal cathode and separator disc, were dried under vacuum at 100 °C before being transferred to an argon-filled glovebox. Due to the air-sensitive nature of the cathode and electrolyte, all subsequent cell preparation was conducted inside the glovebox.

More specifically, the cells being prepared were in fact half-cells. Lithium metal was used in place of another intercalation material (e.g., $LiCoO_2$) to provide the maximum Li^+ ion flux during discharge. Since the cells are cycled in the limit of maximum ion flux, their performance depends upon the active material being tested, rather than a combination of the active material and the cathode.

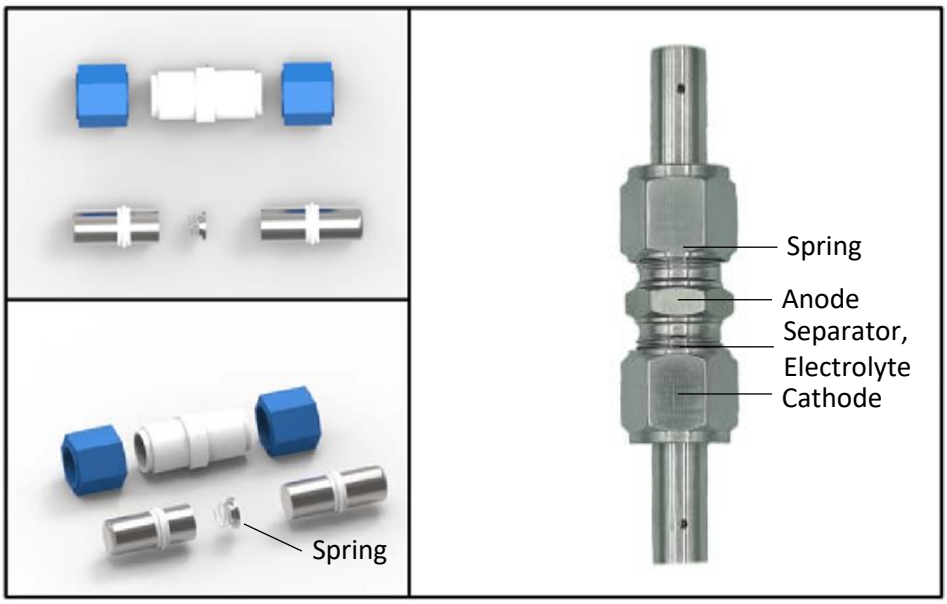

Figure **2.3: Components of a Swagelok™ cell (left) and a fully**-constructed cell (right). In this configuration, the anode, separator, electrolyte and cathode are in close contact, held in place by a stainless steel spring and two stainless steel rods at either end.

2.2.3 Electrochemical Tests

All electrodes were cycled against lithium metal with 1 M $LiPF_6$ in EC:DMC (ethylene carbonate /dimethyl carbonate in a 1:1 volume ratio), obtained from Sigma Aldrich, as the electrolyte. Galvanostatic discharge-charge curves were recorded on a VMP3 multi-channel potentiostat and a cyclic channel SP-150 system from Bio-Logic Science Instruments. The cells were discharged at either 0.5 C or 4 C to a lower limit of 10 mV and recharged to 2.5 V. Data were recorded every 5 mV.

Some of the cells were tested with the intent to study the structure of the active material. Hence, after electrochemical cycling, cells were disassembled inside the glovebox to ensure the active material was preserved. A membrane separator (Celgard) was added to these cells, which ensured the safe removal of the electrodes and the active material. The anodes were washed with DMC and dried for two hours under vacuum at 40 °C before being packed into Kel-F disposal inserts. The inserts were then placed inside a 4 mm zirconium rotors with and analysed via solid-state NMR (vide infra).

2.3 Nuclear Magnetic Resonance Spectroscopy

2.3.1 Principles of Nuclear Magnetic Resonance Spectroscopy[98–100]

Nuclei possess an intrinsic angular momentum called spin, represented by the spin quantum number, I. The magnitude of the spin angular momentum vector, I, is quantised:

$$|\mathrm{I}| = \hbar\sqrt{I(I+1)} \tag{2.3}$$

The spin quantum number may take half-integer and integer values. The angular momentum vector, I, has 2I +1 projections onto an arbitrary axis (commonly the z-axis). Since both its magnitude and direction are quantised, the z-component of the angular moment vector is given by:

$$I_z = m_I\hbar\ , \tag{2.4}$$

where m_I is the magnetic quantum number, which itself has 2I +1 integral values and ranges from -I to +I.

A nucleus with non-zero spin has a magnetic diploe moment, μ, which is also quantised. The gyromagnetic ratio, γ, which is the ratio of the magnetic moment to the angular momentum and is fixed for a given nucleus, determines whether the orientation of the magnetic dipole moment is parallel or anti-parallel to the spin angular momentum vector. For nuclei where γ is positive, the orientation of these vectors is parallel to one another; similarly, for nuclei where γ is negative, they are anti-parallel.

In the absence of a magnetic field, all orientations of the spin angular momentum are degenerate (the same) in energy. This degeneracy is lifted by the application of a strong external magnetic field, B_0. This is known as the Zeeman interaction. The energy of a given state, with dipole moment μ, is given by:

$$E = -\mu \cdot \mathrm{B}_0 \tag{2.5}$$

If the external magnetic field is applied along the z-axis, then:

$$E = -\mu_z \mathrm{B}_0 \tag{2.6}$$

where μ_z is the projection of the dipole moment onto the z-axis and B_0 is the strength of the magnetic field. Therefore, for any magnetic quantum number, combining equations 2.4 and 2.6 shows that the states of the nuclear spin are equal spaced in energy in the presence of a strong magnetic field:

$$E_{|m_I\rangle} = -\gamma m_I \hbar B_0 \tag{2.7}$$

Since the spectroscopic selection rule in nuclear magnetic resonance is $\Delta m_I = \pm 1$, all allowed transitions between nuclear spin states have the same energy:

$$\Delta E = -\gamma \hbar B_0 \tag{2.8}$$

with the associated frequency known as the Larmor frequency, ω_0, reported in Hz:

$$v_0 = \frac{\Delta E}{\hbar} = -\gamma B_0 \tag{2.9}$$

The Larmor frequency of each nucleus is affected by it's chemical environment. The chemical shift arises from the applied magnetic field causing the electrons in the sample to circulate and generate an internal magnetic field, typically denoted B_1. This magnetic field may opposed the applied field, B_0,

generating a diamagnetic current, or add to the applied field, inducing a paramagnetic current. The magnetic field at a select nucleus is then:

$$B_{eff} = B_0 - B_1 = B_0(1 - \sigma) \tag{2.10}$$

where σ is the shielding constant and B_{eff} is the effective field experienced by the nucleus. An atomic nucleus is said to be shielded from the external magnetic field when B_1 opposes B_0 and deshielded when B_1 adds to B_0. Hence, the resonance frequency of the nucleus in the presence of an external magnetic field is given can then be described by

$$\omega = -\gamma B_0(1 - \sigma)\ . \tag{2.11}$$

The shielding is dependent upon the electron density at the nucleus. As a result, many heavy metal nuclei (such as ^{93}Nb) can experience chemical shifts of up to thousands of ppm (e.g., 10,000 ppm).

2.3.2 The NMR Experiment

When the degeneracy of nuclear spin states is lifted by the Zeeman interaction, the relative populations of the spin states is also altered. This leads to the formation of a bulk magnetisation vector, M_0, due to the slight excess of spins in the lower energy state, as predicted by the system's Boltzmann distribution. In the vector model, the nuclear spins are represented as precessing around M_0 at the Larmor frequency.

In an NMR experiment, a short, high-power burst of radio-frequency (RF) radiation, known as a pulse, is applied at the Larmor frequency of the target nuclei. The pulse has a flip angle (in degrees), which describes the angle through which the bulk magnetisation vector is rotated, and a phase, which describes the axis along which the pulse is applied. For the duration of the pulse, the bulk magnetisation vector will precess around this axis. For example, a 90° pulse applied along x will cause M_0 to rotate 90° around the x-axis, after which it will begin to precess around the axis of the external magnetic field once again. This generates a slowly-decaying oscillatory voltage in the spectrometer's receiver coil, which is recorded as a free induction decay (FID). The FID contains information on the frequencies and intensities of all resonances excited by the RF pulse. After Fourier transformation (a mathematical operation which decomposes a function of

time into its constituent frequencies), the FID is converted into a frequency-domain spectrum, where in the x-axis is typically given in parts per million (ppm) instead of Hz for simplicity.

2.3.3 Solid-State NMR

Solution-state NMR experiments typically yield spectra containing sharp, narrow resonances. On the other hand, the study of solids using NMR yields spectra containing very broad lines which, at first glance, appear to offer very little useful information. This line broadening occurs due to a number of mechanisms, including: (1) the dipolar interaction – a through-space interaction whereby a nucleus induces a magnetic field at another nucleus, (2) chemical shift anisotropy (CSA) – the dependence of the chemical shift on the orientation of the nucleus, and (3) the quadrupolar interaction – the interaction of a nuclear quadrupole moment with the electric field gradient (occurs only for nuclei where $I > ½$).

2.3.3.1 Dipolar Coupling

For each nucleus with a magnetic dipole moment, there is a small, localised magnetic field centred upon that nucleus. The strength of this field is denoted B_μ. This field interacts with the dipole moments of nearby nuclei, and the strength of this interaction is affected by their relative strengths, and the distance and geometry between them. Dipolar couplings can be significant in magnitude, often on the order of 10^3 Hz.

2.3.3.2 Chemical Shift Anisotropy

As discussed above, the frequency which a nucleus resonates depends upon its chemical environment. In a liquid sample, where molecules are in a constant state of rotation and translation, the directional and orientational components of the chemical shift are averaged out to an isotropic (directionally independent) value. In a solid, however, this tumbling motion is not present. The shielding or de-shielding effect a neighbour nucleus has on a resonant nucleus therefore becomes dependent upon the distance and

geometry between them. The strength of this interaction is dependent on the term $1 - 3\cos^2\theta$.

2.3.3.3 Quadrupolar Coupling

Nuclei with a spin quantum number greater than I = ½ possess a nuclear quadrupole moment, eQ. This interacts with the electric field generated by other atoms present in the sample. It is an anisotropic (directionally dependent) interaction and in most cases is the dominating interaction present in an NMR experiment, resulting in the inhomogeneous broadening of the spectrum.

The anisotropy of the interaction is described by a tensor (an N-dimensional matrix), or pictorially represented as an ellipsoid. The magnitude of the quadrupolar interaction is proportional to the length of the tensor, given in Hz by the equation

$$C_Q = \frac{eQV_{zz}}{h}\,, \tag{2.12}$$

where C_Q is the quadrupolar coupling constant, V_{ZZ} is the length of the ellipsoid. V_{zz} is also a component of the tensor's principal axis system (PAS) and can be thought of as the length along z-axis. Larger values of C_Q represent stronger quadrupolar interactions. In addition, the cross-section of the ellipsoid provides information about the symmetry of the quadrupolar interaction, which is given by the term η_Q,

$$\eta_Q = (V_{xx} - V_{yy})/V_{zz}\,, \tag{2.13}$$

where V_{xx}, V_{yy} and V_{zz} are all three components of the PAS and $0 < \eta_Q < 1$. An η_Q value of 0 implies that the quadrupolar interaction is the same in all directions, i.e., a symmetrical chemical environment.

2.3.3.4 Magic-Angle Spinning

Due to molecular tumbling in liquids, solution-state NMR spectra often exhibit narrow, distinct lineshapes, enabling the extracting of detail structural information. In solids, however, the interactions discussed above are present simultaneously. This creates much broader lineshapes from which little, if any,

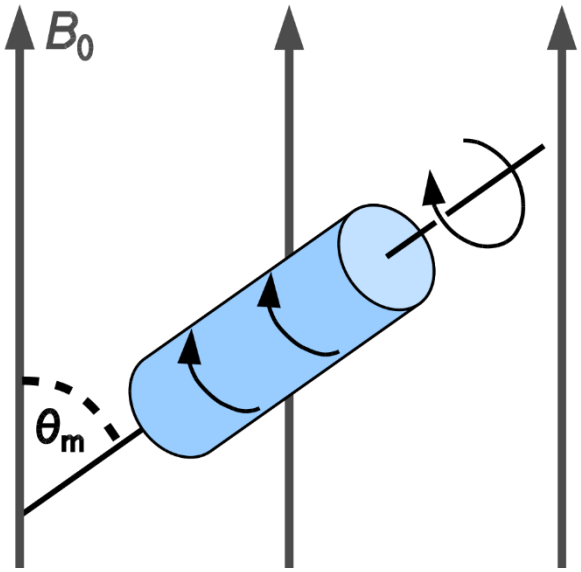

Figure 2.4: A pictorial representation of magic-angle spinning. The sample (blue) is rotated at a high frequency inside the main magnetic field (B_0), rotated at an angle of $\boldsymbol{\theta}_m$.

information can be deduced. However, there are techniques that are commonly employed to suppress these anisotropic interactions.

Magic-angle spinning (MAS) is one such method. During an MAS NMR experiment, the sample is orientated at an angle of 54.736° (one of the solutions to the expression $0 = 1 - 3\cos^2\theta$) relative to the external magnetic field. The sample is then rotated, usually at a frequency between 1 and 130 kHz, dependent upon the mass of the sample and the diameter of the rotor. This is represented in Figure 2.4. Spinning the sample at this angle imitates the motion of molecular tumbling and effectively cancels out the anisotropic interactions, providing the MAS rate is equal to or greater than the magnitude of the interaction being removed. At slow spinning rates the spectrum will exhibit a manifold of peaks evenly spaced out at the MAS rate from the isotropic signal. These peaks are termed spinning sidebands. However, magic-angle spinning does not cancel out the effects of the quadrupolar interaction. The lineshapes observed in MAS NMR experiments are still broadened by the quadrupolar interaction, if it is present, although useful structural information can be reliably obtained from these spectra. To remove this interaction entirely, two-dimensional methods must be employed.

2.3.4 Experimental Procedure

All solid-state NMR spectra were acquired using a Bruker 500 Avanace III spectrometer with a 11.7 T magnet, using Larmor frequencies of 73.600 MHz for ^{6}Li and 194.370 MHz for ^{7}Li. Each sample was prepared (vide supra) under an argon atmosphere and packed into inserts for 4 mm zirconium rotors. The MAS rate used was 10 kHz. The spectra were analysed using the Bruker TopSpin software.

Chapter 3 Results and Discussion

3.1 Synthesis and Characterisation of $Nb_{16}W_5O_{55}$

Initially, samples of shear-type $Nb_{16}W_5O_{55}$ were synthesised following the co-thermal oxidation method described by Griffith et al.[71] Stoichiometric quantities of WO_3, WO_2 and NbO_2 (obtained from Sigma Aldrich) were ground together by hand in an agate pestle and mortar, then pressed into a pellet (ø = 10 mm) under 10 MPa of pressure in a hydraulic press. The pellets were then fired in an alumina crucible in a furnace at 1473 K (1200 °C) for 2 hrs. The temperature of the furnace was increased at a rate of 10 K min^{-1} and was allowed to cool naturally to room temperature. After this, the pellets crumbled to yield a pale green powder.

To assist in determining the phase composition, PXRD data was obtained and a Rietveld refinement was completed (Figure 3.1). The structural model for $Nb_{16}W_5O_{55}$, obtained as a crystallographic information file from the

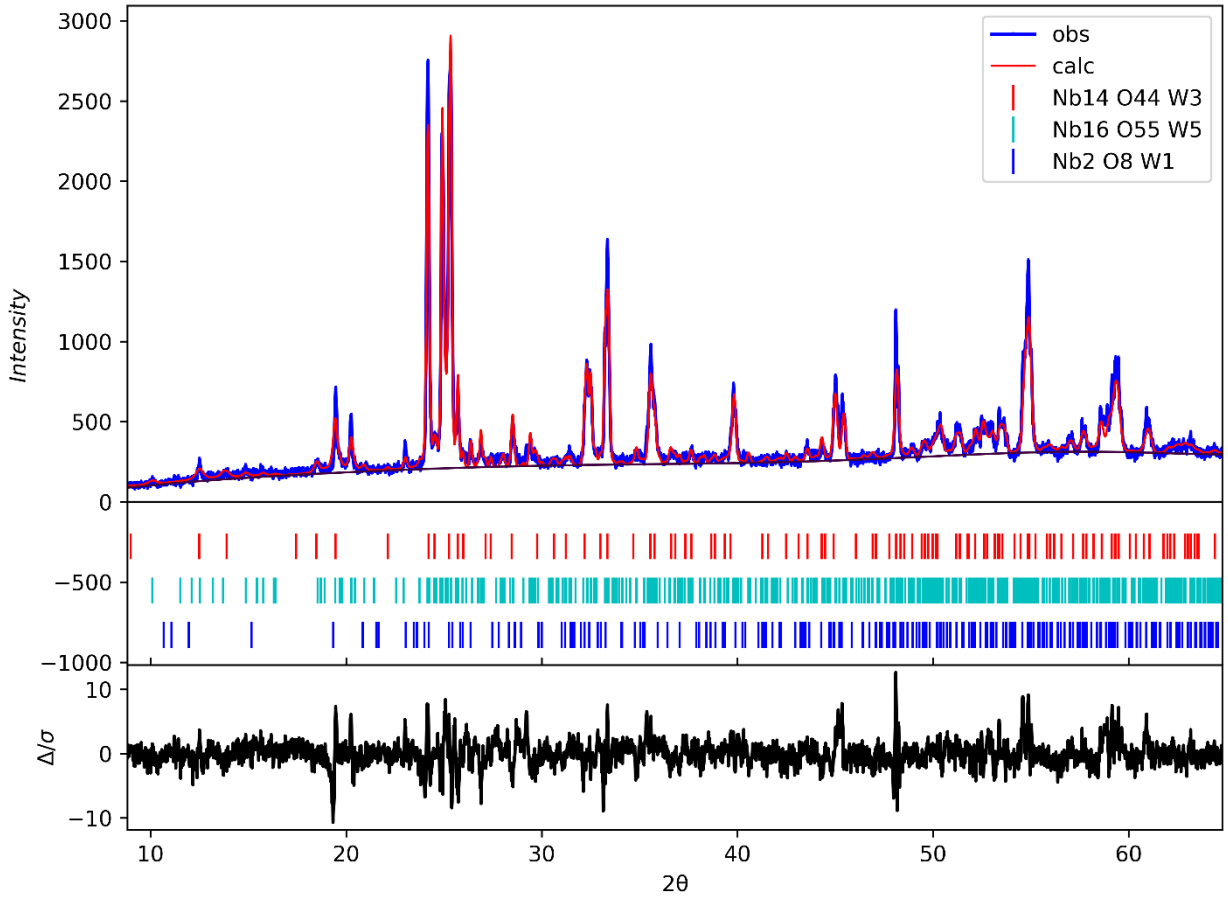

Figure 3.1: Rietveld refinement of the PXRD data obtained from the initial sample of $Nb_{16}W_5O_{55}$. Phase composition: $Nb_{16}W_5O_{55}$ = 70.0%, Nb_2WO_8 = 3.1%, $Nb_{14}W_3O_{44}$ = 26.9%; wRp = 10.8%. The difference between the observed and calculated diffraction patterns is shown in black in the lower portion of the plot.

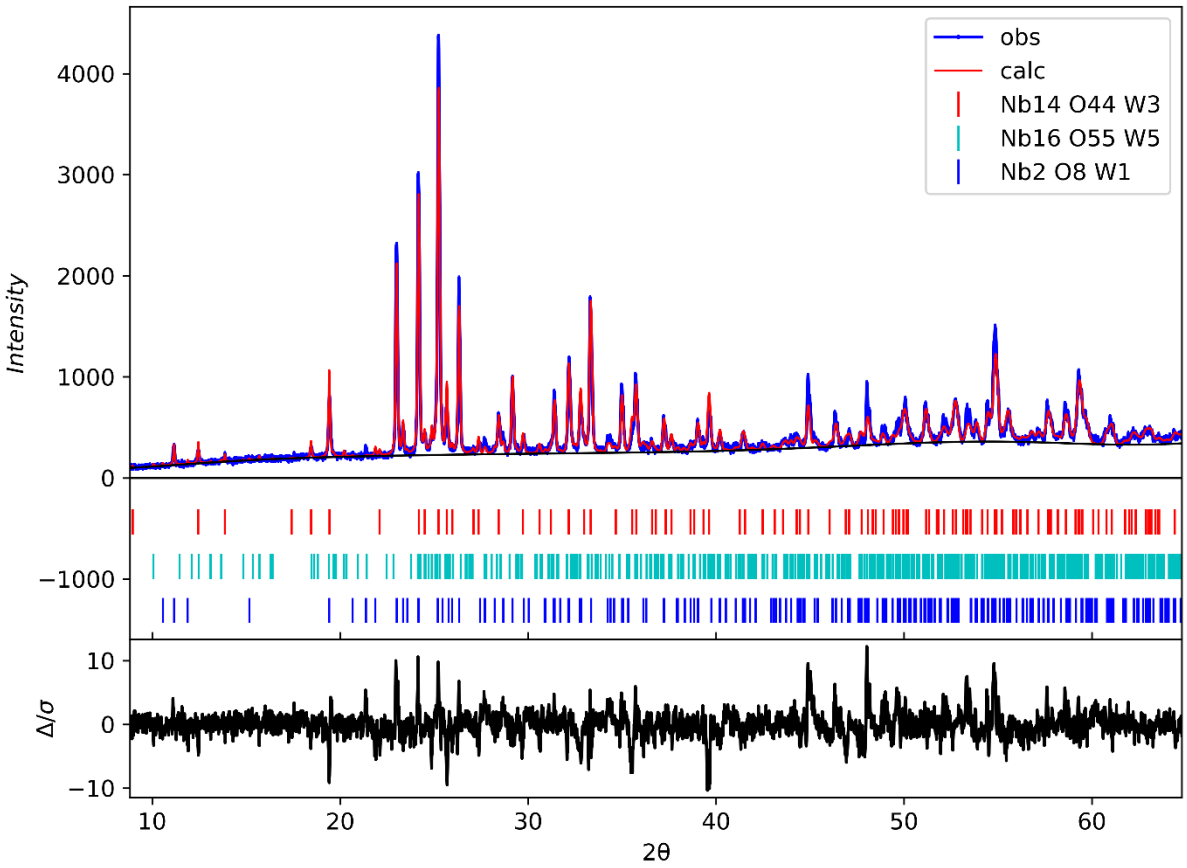

Figure 3.2: Rietveld refinement of the PXRD data obtained from the initial sample of $Nb_{16}W_5O_{55}$ after being heated for an additional 2 hours. Phase composition: $Nb_{16}W_5O_{55}$ = 10.1%, Nb_2WO_8 = 40.7%, $Nb_{14}W_3O_{44}$ = 49.2%; wRp = 10.1%. The difference between the observed and calculated diffraction patterns is shown in black in the lower portion of the plot.

ICSD, was used as the primary phase in the refinement, along with the reported disproportionation products, Nb_2WO_8 and $Nb_{14}W_4O_{44}$. Reasonably good agreement between the calculated and experimental diffraction patterns was observed (wRp = 10.8%). The Rietveld refinement suggests that the dominant phase in the sample is $Nb_{16}W_5O_{55}$, with a phase fraction of 70.0 wt%; the remaining 30.0% of the sample consisted of $Nb_{14}W_3O_{44}$ (26.9 wt%) and Nb_2WO_8 (3.1 wt%). According to Roth, $Nb_{16}W_5O_{55}$ is a metastable phase formed between 1363 and 1658 K, and upon cooling should disproportionate to $Nb_{14}W_3O_{44}$ and Nb_2WO_8, hence the choice of phases used in this Rietveld refinement.[75]

The sample was then milled by hand and reheated for an additional 2 hrs at 1473 K to investigate the effect of further sintering on the phase purity of the sample. However, the diffractogram shown in Figure 3.2 appears to indicate that the phase composition changed dramatically after being reprocessed. More specifically, many additional diffraction peaks are now present in the diffraction pattern and, using the same structural models as

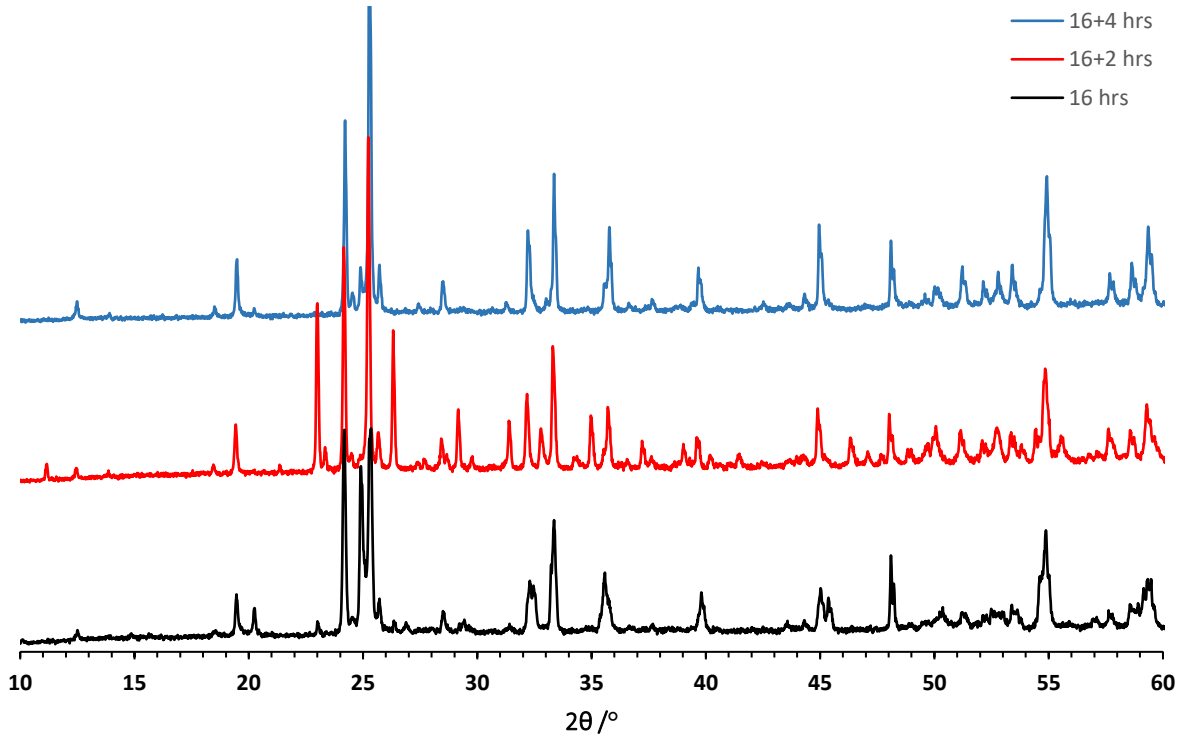

Figure 3.3: Evolution of the diffraction pattern for the initial sample of $Nb_{16}W_5O_{55}$ after heating the powder two additional times. Black – initial synthesis; red – after milling and +2 hrs of heating; blue – after milling and +4 hrs (total) of heating

before, the Rietveld refinement indicates that the phase fraction of $Nb_{16}W_5O_{55}$ has decreased significantly to 10.1 wt%. At the same time, the phase fractions of $Nb_{14}W_3O_{44}$ and Nb_2WO_8 increased to 49.2 wt% and 40.7 wt%, respectively. After another 2 hrs of sintering at 1473 K (total additional sintering time of 4 hrs), the $Nb_{14}W_3O_{44}$ phase became the dominant phase, with a phase fraction of 78.3 wt%. The Rietveld refinement for this sample is shown in Supplementary Information, Figure S.1. The evolution of the diffraction pattern as a function of sintering time is shown in Figure 3.3. The PXRD data presented suggests that the metastable $Nb_{16}W_5O_{55}$ phase is formed at high temperatures and short reaction times, and that the cooling process directly and irreversibly yields the disproportionation products. However, Roth and Wadsley report that both initial heat treatment at 1623 K and quickly cooling the products (quenching) results in the preparation of phase-pure samples of $Nb_{16}W_5O_{55}$.[77] Unfortunately, due to furnace limitations, i.e., the lack of a furnace capable of reaching these extreme temperatures, the method could not be attempted in our laboratory or department.

To determine the effects of pressure on the phases formed, the initial synthetic procedure was repeated using non-pelletised reagent powders.

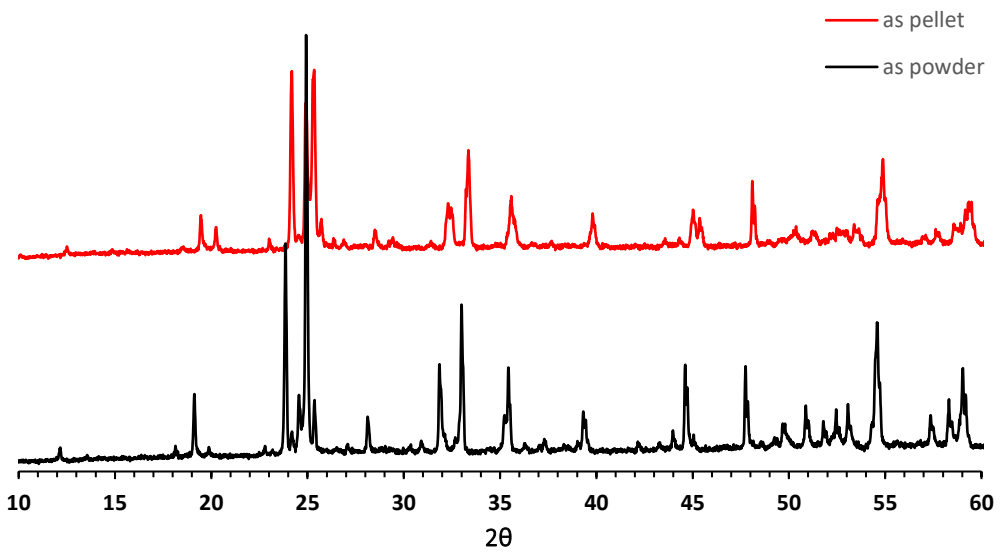

Figure 3.4: Comparison of the diffraction patterns obtained from samples synthesised as powders (in black) and as pellets (in red).

PXRD data was obtained for the resultant pale green powder, which at a glance appeared the same as the sample produced during the initial synthesis. However, it is noted that the diffraction pattern obtained indicated marked differences to that from the initial synthesis, as shown in Figure 3.4. In particular, certain peaks are more prominent in the diffraction pattern obtained for the sample synthesised from the raw powders. In particular, the peaks at $2\theta \approx 18°$, 22.5° and 32° and 45° exhibit distinct differences in intensities. Rietveld analysis revealed that these peaks correspond to the $Nb_{14}W_3O_{44}$ phase, which in this sample, had a phase fraction of 87.4 wt%. The unit cells of $Nb_{14}W_3O_{44}$ and $Nb_{16}W_5O_{55}$ are shown in Figure 3.5. In this sample, the $Nb_{16}W_5O_{55}$ had a phase fraction of 12.6 wt%. However, the Rietveld analysis, shown in Figure 3.6, had a poor fit (wRp = 15.9%), indicating that there may be additional and unknown phases present in the sample, not including the Nb_2WO_8 phase which usually accompanies $Nb_{14}W_3O_{44}$ as a product of the disproportionation of $Nb_{16}W_5O_{55}$. Therefore, it can be concluded that synthesising $Nb_{16}W_5O_{55}$ as a pellet appears to suppress the mechanism by which disproportionation occurs. This may be due to the close proximity of individual grains with the pellet suppressing the mechanism of disproportionation, either by preventing the crystallite from rotating or moving on a molecular level or by providing very little space for the products of disproportionation. Due to the small difference in free energy between the two phases, even a small change in synthetic conditions may have a major effect

on the phase purity of the sample, or the specific phases that are formed, as demonstrated here.

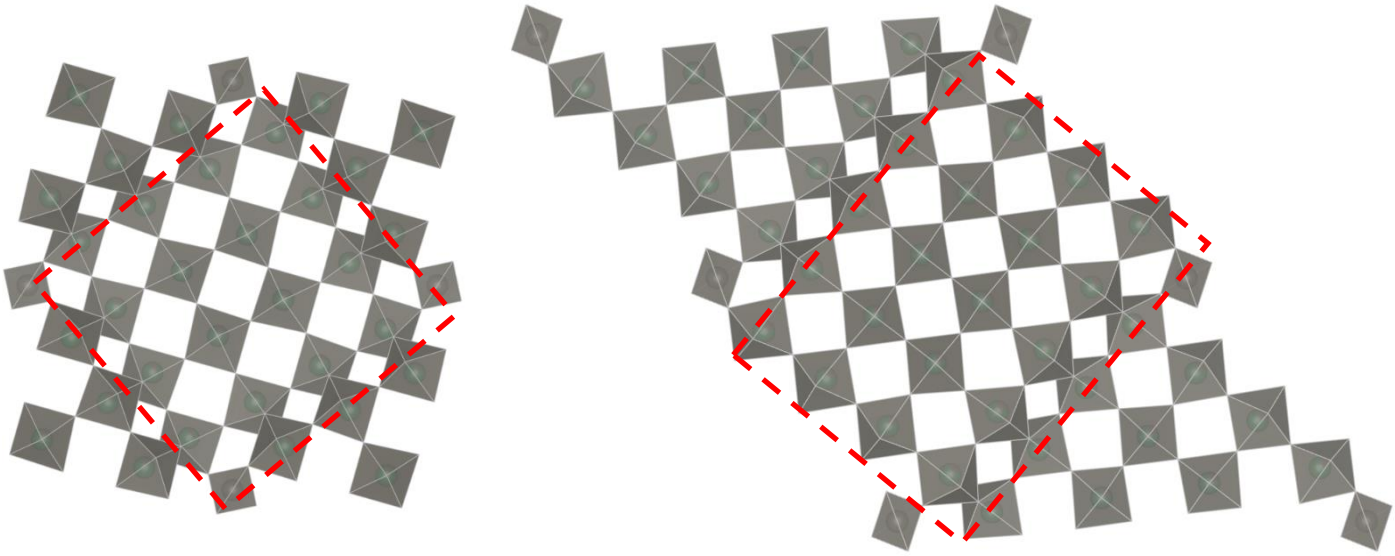

Figure 3.5: Comparison of the unit cells of $Nb_{14}W_3O_{44}$ (left) and $Nb_{16}W_5O_{55}$ (right). The block structure of each is shown in red. The $Nb_{14}W_3O_{44}$ phase is composed of [4 x 4] blocks, whilst the $Nb_{16}W_5O_{55}$ phase is composed of [5 x 4] blocks.

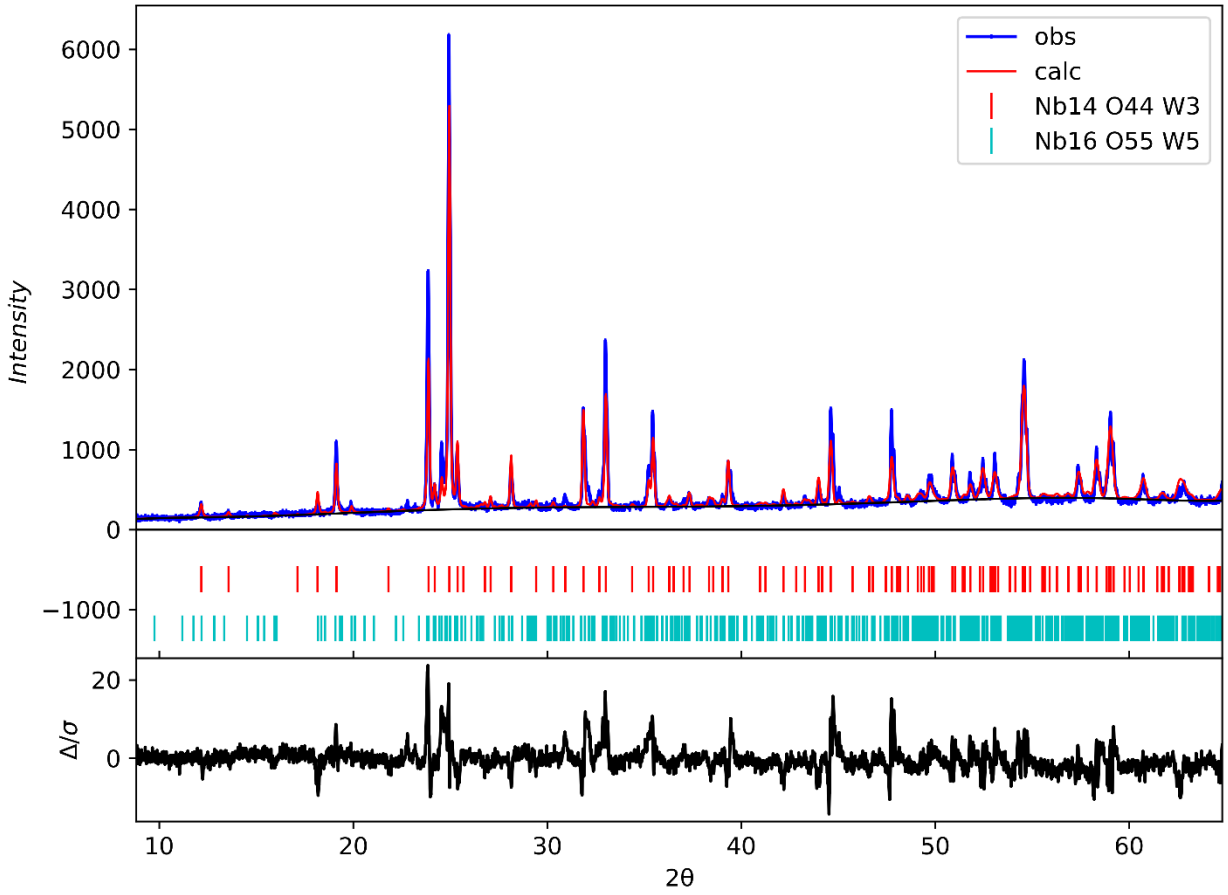

Figure 3.6: Rietveld refinement of the sample of $Nb_{16}W_5O_{55}$ synthesised as a raw powder, without being pelletised. Phase composition: $Nb_{14}W_3O_{44}$ = 87.4%, $Nb_{16}W_5O_{55}$ = 12.6%; wRp = 15.9%. The difference between the observed and calculated diffraction patterns is shown in black in the lower portion of the plot.

3.2 $Nb_{6.7}W_{10.3}O_{47}$

3.2.1 Synthesis and Characterisation

Samples of block- type $Nb_{6.7}W_{10.3}O_{47}$ were synthesised following the co-thermal oxidation method described by Griffith et al.[71] Stoichiometric quantities of WO_3, WO_2 and NbO_2 (obtained from Sigma Aldirch) were ground together by hand in an agate pestle and mortar, then pressed into a pellet (ø = 10 mm) under 10 MPa of pressure in a hydraulic press. The pellets were then fired in an alumina crucible in a furnace at 1473 K (1200 °C). The temperature of the furnace was increased at a rate of 10 K min^{-1} and was allowed to cool naturally after 2 hrs. After this, the pellets crumbled to yield an off-white powder.

To assist in determining the phase composition, PXRD data was obtained and a Rietveld refinement was completed (shown in Figure 3.7). The structural model for $Nb_{6.7}W_{10.3}O_{47}$, obtained as a crystallographic information file from the ICSD, was used as the primary phase in the refinement. The

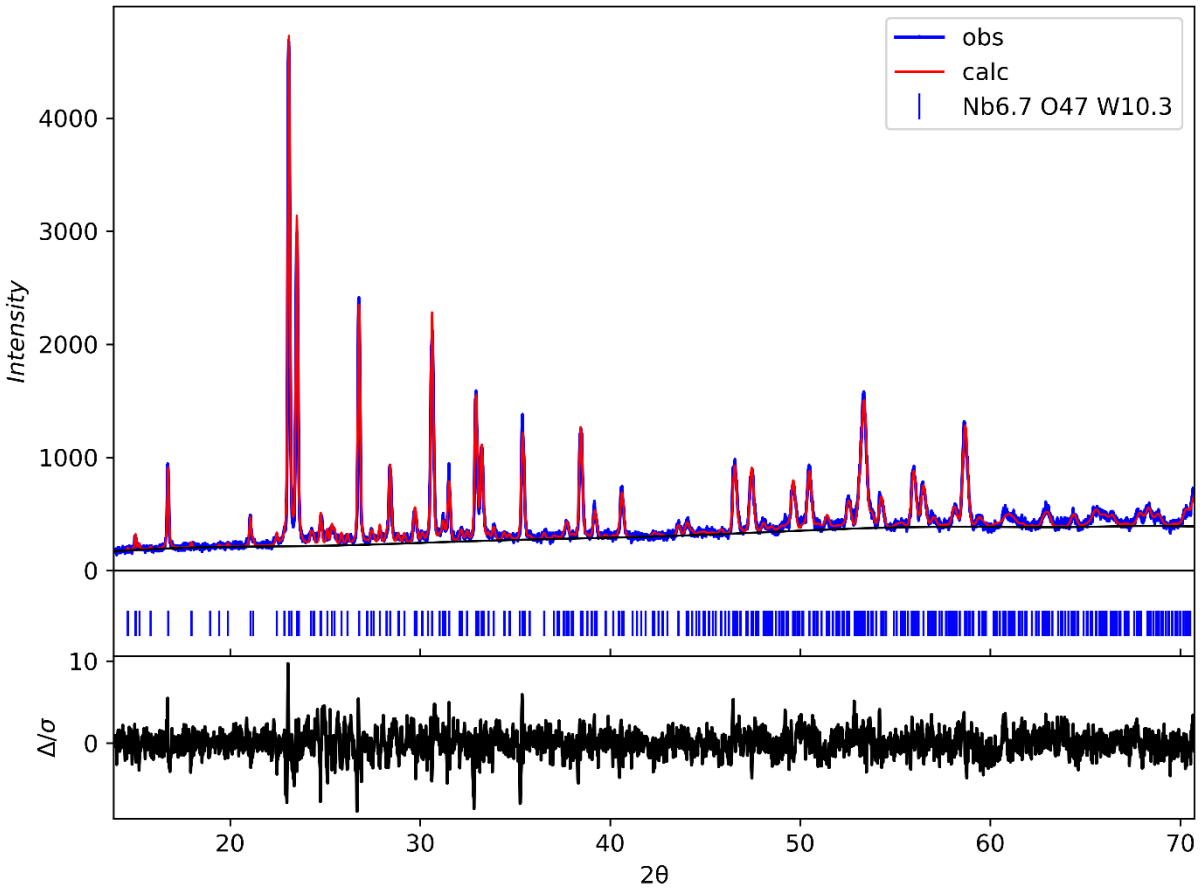

Figure 3.7: Rietveld refinement of the PXRD data obtained for a sample of $Nb_{6.7}W_{10}O_{47}$ prepared at 1473 K for 2 hrs. Only the $Nb_{6.7}W_{10}O_{47}$ phase was present (wRp = 7.22%). The difference between the observed and calculated diffraction patterns is shown in black in the lower portion of the plot.

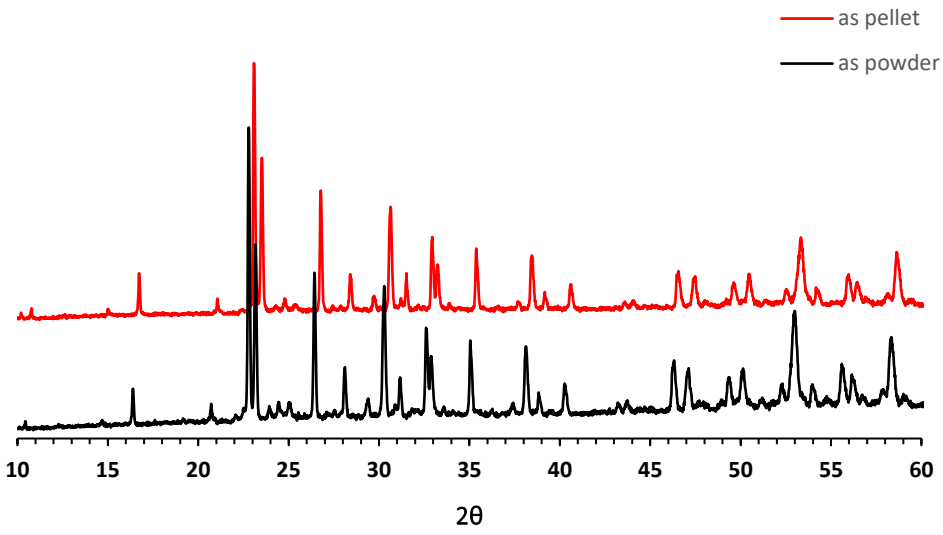

Figure 3.8: Comparison of the X-ray diffraction patterns obtained for $Nb_{18}W_{16}O_{93}$ (black, synthesised as a powder) and $Nb_{6.7}W_{10.3}O_{47}$ (red, synthesised as a pellet). There is a slight contraction in the unit cell along the c-axis, as well as increased intensity in the peaks at 2θ = 24° and 25°.

phase composition was determined to be primarily $Nb_{6.7}W_{10.3}O_{47}$ with a wRp of 7.22%. Other phases were considered in concurrent Rietveld refinements, such as the $Nb_{18}W_{16}O_{93}$ phase, which has a very similar structure. The refinement carried out using the structural model for $Nb_{18}W_{16}O_{93}$ provided an acceptable fit, however, there were noticeable differences between the calculated diffraction pattern and the experimental data in the region of 22-26°. These differences were not present when the refinement was carried out with the $Nb_{6.7}W_{10.3}O_{47}$ phase.

In a similar manner to $Nb_{16}W_5O_{55}$, the initial synthetic procedure was repeated using raw reagent powders (i.e., they were not pressed into pellets before being sintered). The resultant powder was off-white in colour. It appeared identical to the powder synthesised as a pellet, however, the PXRD data showed some differences, as highlighted in Figure 3.8. Along with a slight contraction of the unit cell along the c-axis, as revealed by the Rietveld analysis, two small peaks in the region of 2θ = 24-26° exhibited an increase in intensity. Rietveld refinement using the $Nb_{18}W_{16}O_{93}$ structural model provided better agreement with the observed diffraction pattern than with $Nb_{6.7}W_{10.3}O_{47}$ and indicated the presence of a $Nb_{18}W_{16}O_{93}$ phase (wRp = 8.80%). However, subsequent efforts to synthesise $Nb_{18}W_{16}O_{93}$ were unsuccessful, highlighting the difficulty in preferentially synthesising one phase over the other. Given the similarities between $Nb_{6.7}W_{10.3}O_{47}$ and $Nb_{18}W_{16}O_{93}$, it is possible that the samples produced here consist of a mix of

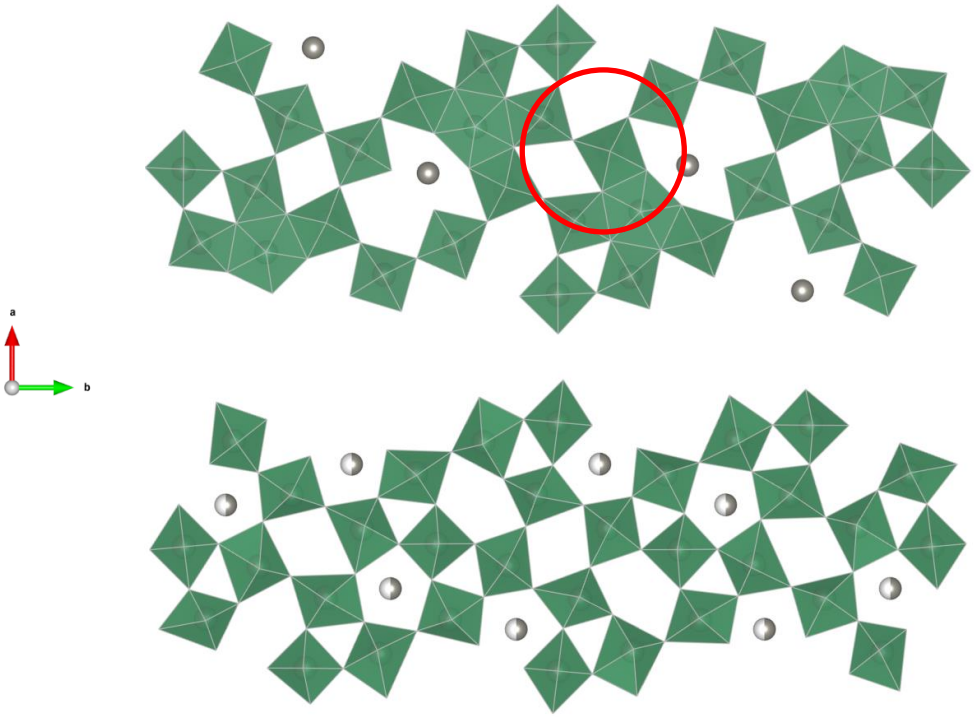

Figure 3.9: Comparison of the unit cells of $Nb_{6.7}W_{10.3}O_{47}$ (top) and $Nb_{18}W_{16}O_{93}$ (bottom). The green polyhedral represent NbO_6 octahedra. The grey spheres sites fully or partially occupied by W atoms.

the two. Figure 3.9 shows a comparison of the unit cells of $Nb_{6.7}W_{10.3}O_{47}$ and $Nb_{18}W_{16}O_{93}$ to illustrate these similarities. Alongside the more even distribution of tungsten throughout the channels in the NbO_6 framework, tungsten atoms in $Nb_{18}W_{16}O_{93}$ only occupy pentagonal sites in the structure. On the other hand, in $Nb_{6.7}W_{10.3}O_{47}$ tungsten only occupies the quadrangular sites adjacent to the pentagonal channels, as highlighted in red. Based on the sensitivity shear-type niobium tungsten oxides exhibit towards the precise synthetic conditions, these small differences in the unit cell may be enough to cause one structure to be preferentially formed over the other, or for both phases to co-exist in a similar manner to Wadsley defect fringes in the $Nb_{16}W_5O_{55}$ system.

3.2.2 Probing the Electrochemical Behaviour of $Nb_{6.7}W_{10}O_{47}$

Half-cells containing $Nb_{6.7}W_{10.3}O_{47}$ as the active material were prepared and tested to determine their electrochemical behaviour. The half cells were initially discharged at a rate of 0.5 C and 4 C. Figure 3.10 displays the galvanostatic discharge obtained for $Nb_{6.7}W_{10.3}O_{47}$ at 4 C and 0.5 C. Fewer Li^+ ions were intercalated at 4 C. Only 59.6 Li^+ ions were intercalated per formula unit of $Nb_{6.7}W_{10.3}O_{47}$ at 4 C, whereas 128.9 Li^+ ions were inserted per formula unit at 0.5 C. At higher rates of discharge, the greater influx of Li^+ ions at the surface of the electrode likely caused the SEI layer to build up more immediately, restricting the number of Li^+ ions that can intercalate from the onset. This is seen in the shapes of the discharge curves. In the half-cell discharged at 0.5 C, the three-step intercalation process described by Griffith et al.,[71] wherein the intercalating Li^+ ions preferentially enter the pentagonal, square and triangular channels in the structure, is better defined, occurring

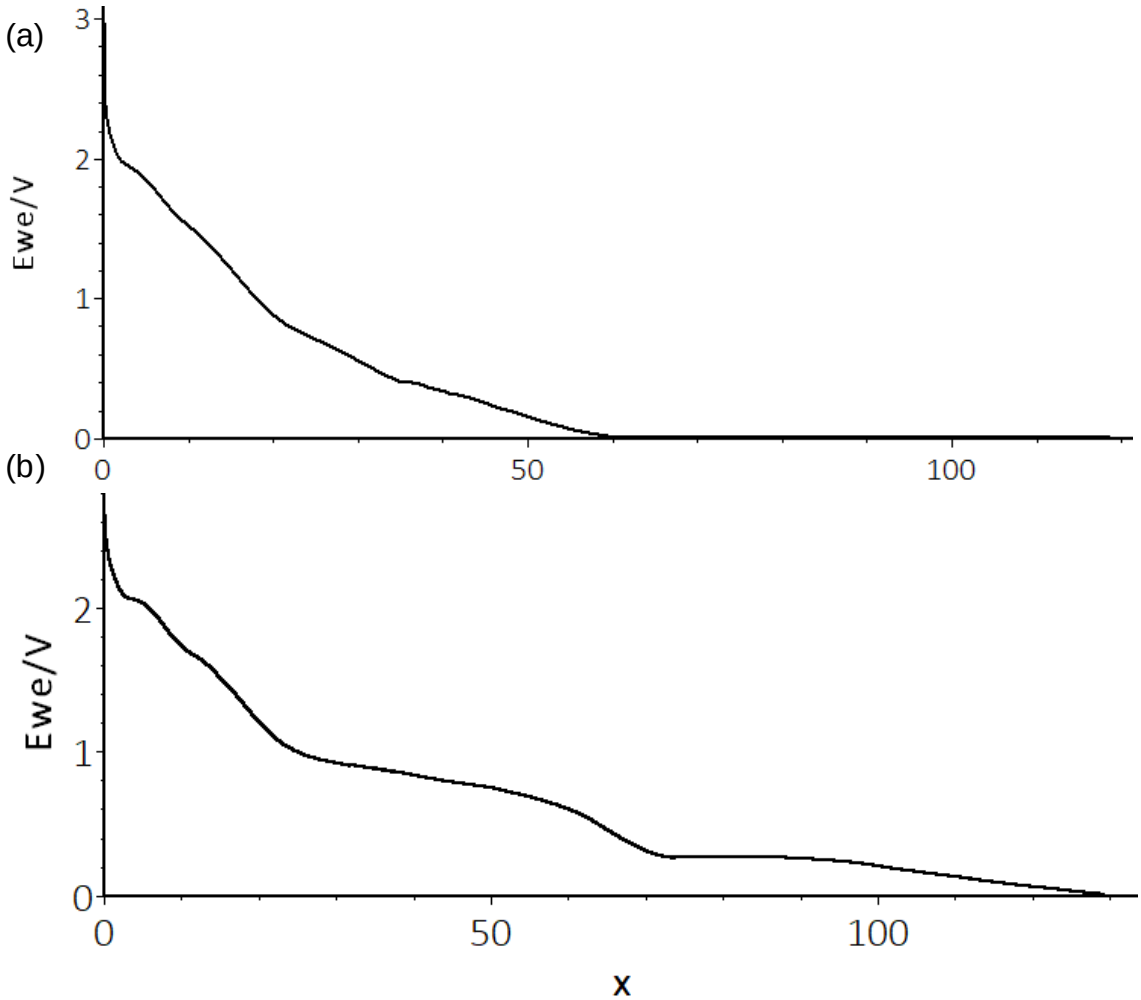

Figure 3.10: (a) Galvanostatic discharge curve for $Nb_{6.7}W_{10.3}O_{47}$, discharged at a rate of 4 C. (b) Galvanostatic discharge curve for $Nb_{6.7}W_{10.3}O_{47}$, discharged at a rate of 0.5 C The x-axis denotes the number of Li^+ ions intercalated per formula unit (x).

between 2.5 V and 1.0 V. Additionally, there appears to be two distinct steps taking place in the 1.0 V to 0.0 V range, likely corresponding to electrochemical process at the surface of the electrode.

A half-cell containing $Nb_{6.7}W_{10.3}O_{47}$ was then cycled at a rate of 0.5 C to the end of its second discharge. Figure 3.11 shows the galvanostatic discharge-charge curve for this half-cell. After charging, 49.9 Li^+ ions per formula unit were recovered from the electrode (out of 128.9), indicating that most of the Li^+ inserted during in the first discharge cycle contributed to the formation of the SEI layer. On the second discharge, 36.2 Li^+ per formula unit were intercalated into the electrode. Similar behaviour was observed for the half-cell discharged at 4 C, wherein approximately 50 Li^+ ions per formula unit remained in the electrode during the charge cycle and 40.2 Li^+ per formula unit were intercalated during the second discharge cycle. When comparing the quantity of Li^+ being inserted into the electrode during discharge to the

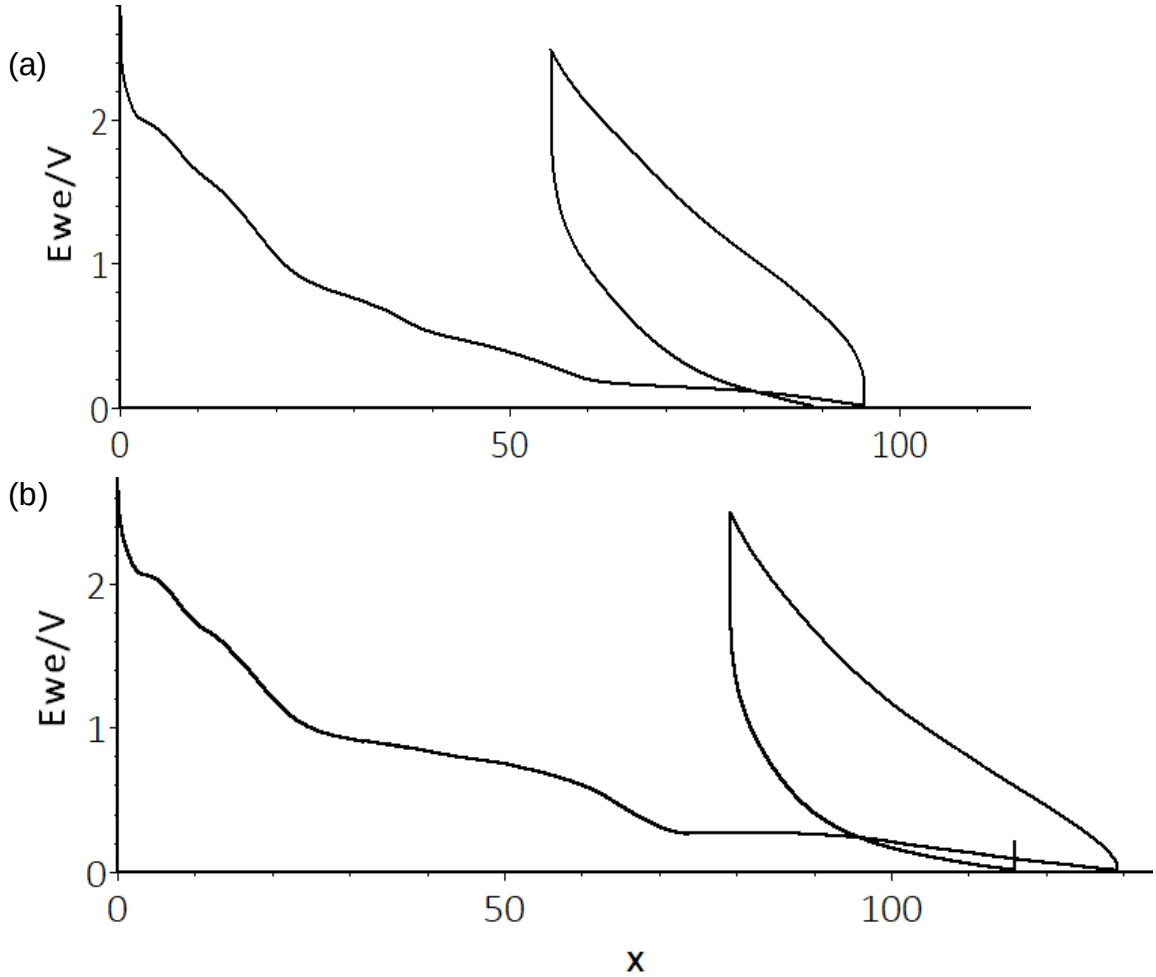

Figure 3.11: (a) Galvanostatic 2nd discharge curve for $Nb_{6.7}W_{10.3}O_{47}$ cycled at 4 C. (b) Galvanostatic 2nd discharge curve for $Nb_{6.7}W_{10.3}O_{47}$ cycled at 4 C. The x-axis denotes the number of Li^+ ions intercalated per formula unit (x).

number of transition metal atoms in one unit cell of $Nb_{6.7}W_{10.3}O_{47}$, the galvanostatic profiles indicate that between 2.13 and 2.36 Li^+/TM are intercalated during discharge. However, this does not preclude the possibility that some of the Li^+ inserted during the second discharge also contributes to the SEI layer; each time an electrochemical cell is cycled, it is expected that some of the Li^+ ions will be lost to the SEI layer.

As a preliminary investigation into the long-term cyclability of $Nb_{6.7}W_{10.3}O_{47}$, a third half-cell was constructed and cycled at a rate of 4 C. It is noted that, due to the extremely long cycling times at 0.5 C in experiments with multiple discharge-charge cycles (> 14 days to reach the 3rd discharge), a half-cell was not cycled at 0.5 C. The galvanostatic discharge-charge curves

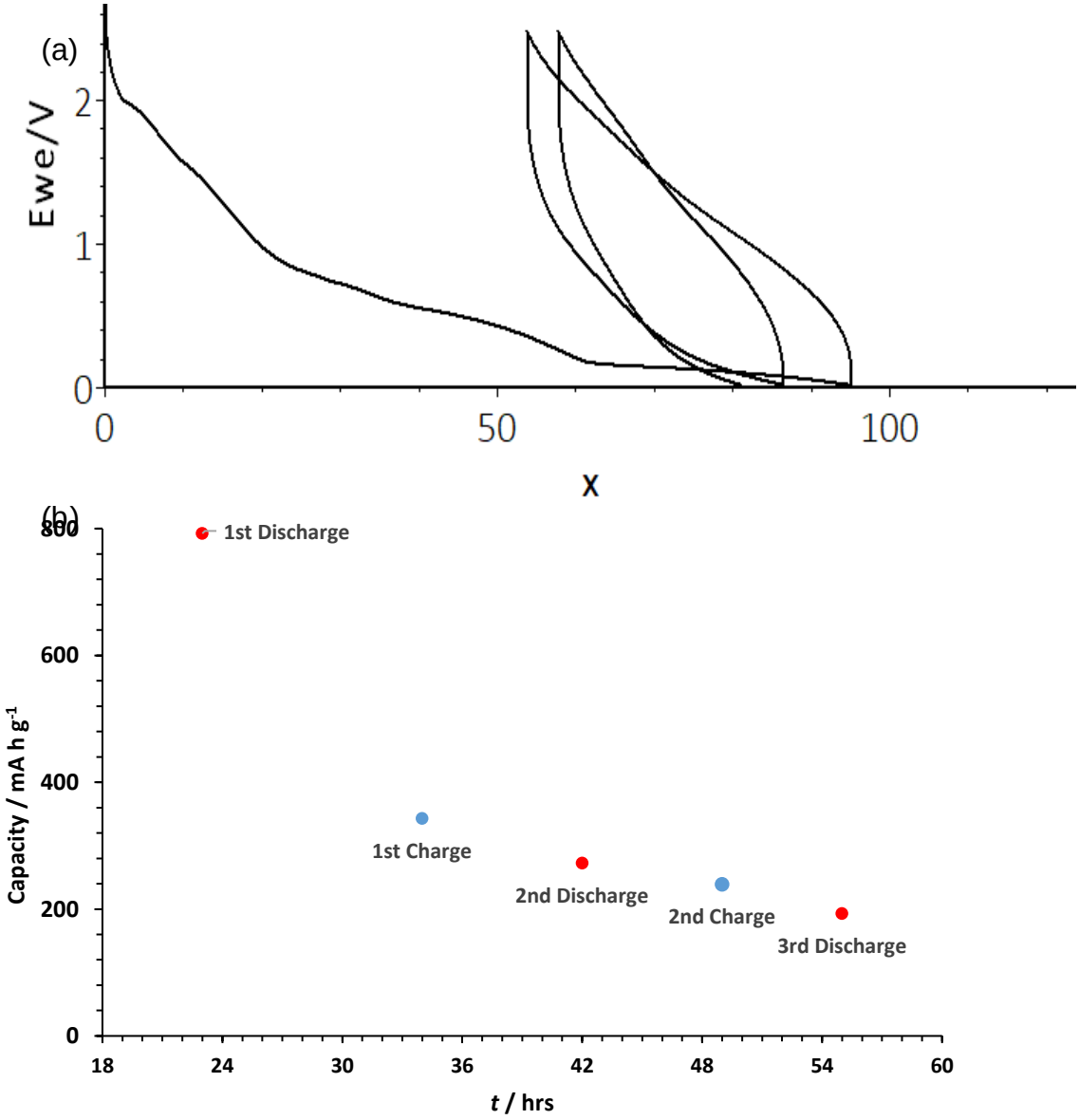

Figure 3.12: (a) Galvanostatic discharge profile for $Nb_{6.7}W_{10.3}O_{47}$ cycled at 4 C to the end of the 3rd discharge and (b) variation in capacity over time.

for $Nb_{6.7}W_{10.3}O_{47}$ to the end of the 3rd discharge cycle are shown in Figure 3.12. The corresponding capacity of the electrode is also shown in Figure 3.12, showing the potential for capacity fade over multiple discharge-charge cycles. Although a sharp decrease in capacity (down 1.60 Li^+/TM) is expected between the first and second discharge (due to the formation of the SEI layer), the downward trend thereafter indicates that the SEI layer continues to evolve on subsequent cycles and reduces the overall performance of the electrode. However, it is not clear whether this trend continues on subsequent cycles or whether the capacity tends towards a non-zero minimum over time. Additional testing over multiple cycles would be required to confirm this.

3.3 K_xWO_3

3.3.1 Synthesis and Characterisation

Initial samples of potassium tungsten oxide, K_xWO_3 (x = 0.10, 0.13, 0.15), were synthesised based on the method by Hussain and Kihlborg.[92] Each sample was investigated using PXRD. Stoichiometric quantities of WO_3, WO_2 and K_2WO_4 were mixed together and ground by hand in an agate pestle and mortar. The reagents were purchased from Sigma Aldrich, rather than being prepared in the laboratory. The mixture was then placed in an alumina crucible inside a quartz glass tube, which was evacuated using a conventional Schlenk line and heated at 1073 K for 16 hrs. The temperature was increased at a rate of 10 K min^{-1} and the sample was slowly cooled to room temperature inside the apparatus. The resultant powder was grey-green, different in colour to that of the starting mixture.

At first glance, the diffraction patterns obtained for this narrow range of compositions were complex, with multiple peaks clustered around distinct

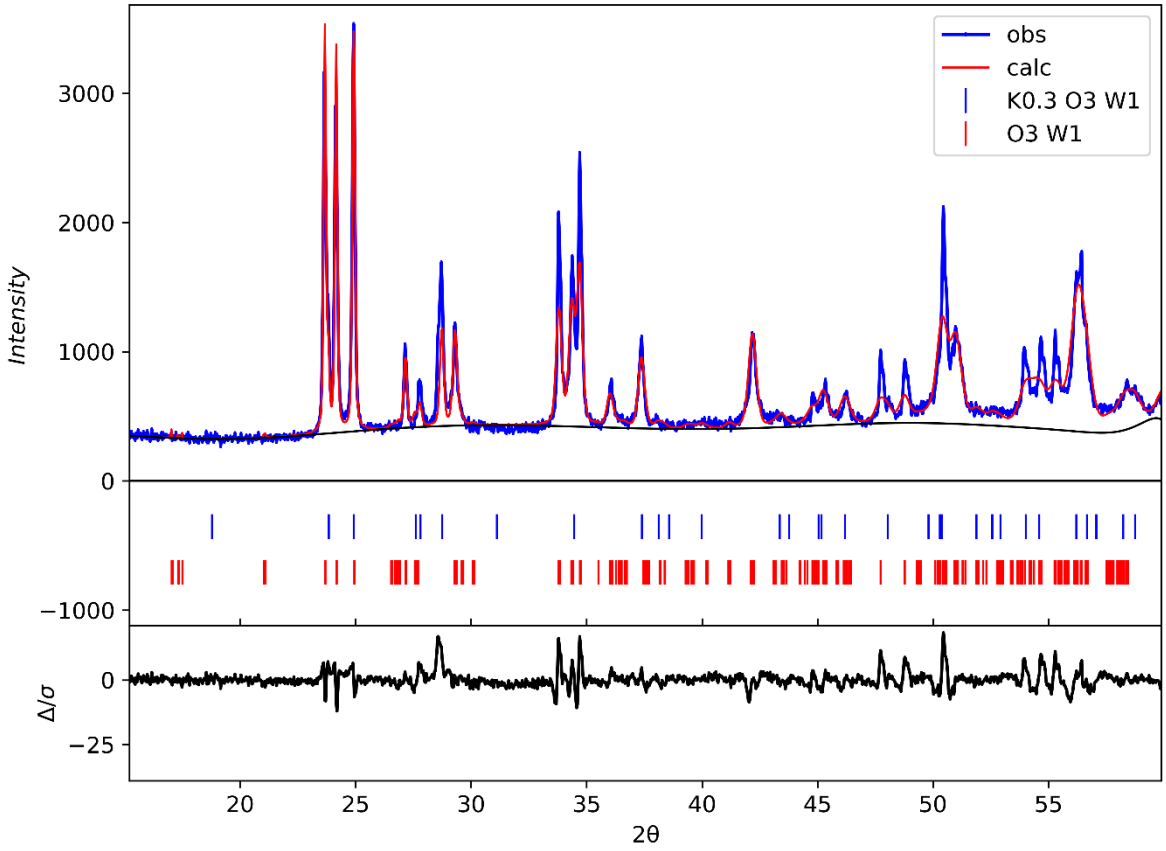

Figure 3.13: Rietveld refinement of the PXRD data obtained from a sample of $K_{0.13}WO_3$ synthesised in a Schlenk line. Phase composition: WO_3 = 89.1%, $K_{0.3}WO_3$ (HTB) = 10.9%; wRp = 12.1%. The difference between the observed and calculated diffraction patterns is shown in black in the lower portion of the plot.

regions of the diffractogram. These clusters were only partially present in the calculated diffraction patterns of $K_{0.3}WO_3$ and WO_3, which represent the end members of the WO_3-HTB series. Therefore, it was predicted that the samples contained both phases in some proportion. The diffraction patterns for each sample in the range were very similar. A Rietveld refinement was carried out on $K_{0.13}WO_3$ sample to assist in phase determination. The structural models for $K_{0.3}WO_3$ (representing the HTB phase) and WO_3 were obtained as crystallographic information files from the ICSD. An acceptable agreement between the observed and calculated diffraction patterns was discovered (wRp = 12.1%), as shown in Figure 3.13. The phase fractions of WO_3 and $K_{0.3}WO_3$ were 89.1 wt% and 10.9 wt% respectively, suggesting that the reaction did not go to completion, although some of the hexagonal phase was synthesised successfully.

Following this, samples of K_xWO_3 (x = 0.05, 0.10, 0.13, 0.25, 0.30, 0.40) were synthesised by sintering the reagent powders in air in a conventional box furnace. The mixed powders were placed in an alumina crucible and heated in a furnace at 1073 K for 16 hrs. The temperature of the furnace was increased at a rate of 10 K min^{-1} and the samples were slowly cooled to room temperature. The resultant powders were yellow-green in colour, strikingly different to those synthesised in a Schlenk line. The diffractograms obtained for these samples were similar to those obtained

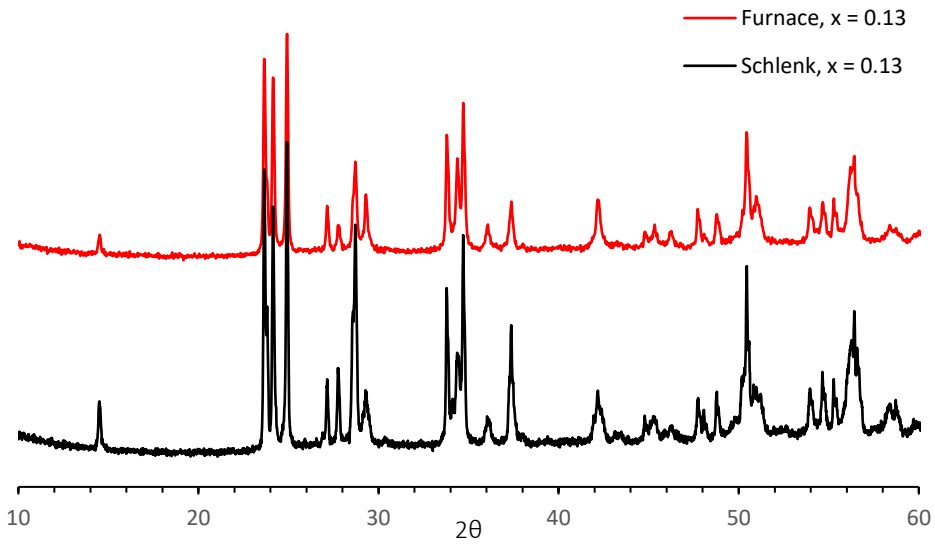

Figure 3.14: Comparison of the X-ray diffraction patterns for $K_{0.13}WO_3$ (synthesised in vacuo using Schlenk apparatus) and $K_{0.13}WO_3$ (synthesised in air). The key differences are the **difference in intensity of the peaks at 2θ ≈ 14°, 28°, 34°, 37° and 51°, corresponding to a higher** fraction of the hexagonal phase. Phase composition for $K_{0.13}WO_3$ (Schlenk): WO_3 = 66.9%, $K_{0.3}WO_3$ (HTB) = 33.1%; wRp = 15.1%

previously, as shown in Figure 3.14. A Rietveld refinement was completed for the $K_{0.13}WO_3$ sample using the same WO_3 and $K_{0.3}WO_3$ (HTB) structural models. The refinement is shown in Supplementary Information, Figure S.2. From the refinement, the phase fractions were 66.9 wt% and 33.1 wt% respectively, i.e., the hexagonal phase was more abundant in this sample than in the $K_{0.13}WO_3$ sample synthesised. However, the residual between the experimental diffraction pattern and the diffraction pattern calculated in this Rietveld refinement was not as good (wRp = 15.1%), indicating that there may have been a phase similar to either WO_3 or $K_{0.3}WO_3$ present in the sample.

It is not clear from the PXRD data alone whether the sample of $K_{0.13}WO_3$ consisted of separate WO_3 and hexagonal K_xWO_3 domains, or if these phases were interlocking as reported by Hussain and Kihlborg.[92] Unfortunately, it was not possible to obtain optical microscopy or HREM data to compare the appearances of these samples with those reported in the literature. Instead, an approach was taken whereby the electrochemical behaviour of $K_{0.13}WO_3$ would be compared to that of WO_3 and hexagonal $K_{0.4}WO_3$, and subsequently Rietveld refinements of the other compositions in the series were not conducted.

3.3.2 Evaluating the Electrochemical Performance of $K_{0.13}WO_3$

$K_{0.13}WO_3$ lies at the upper end of the region of x-values where the ITB is reported to form, as noted by Hussain and Kihlborg.[92] Therefore, in order to establish whether lithium intercalated into a HTB-like environment or into a WO_3-like environment, $K_{0.13}WO_3$ was chosen as the active material; it was predicted that this composition would containing the greatest concentration of hexagonal channels in the ITB phase. Half cells containing $K_{0.13}WO_3$ as the active material were subsequently prepared, and the half cells were discharged and charged at a rate of 0.5 C. For comparison, half cells containing WO_3 and $K_{0.4}WO_3$ (HTB structure) as the active materials were also prepared in order to compare the electrochemical performance of $K_{0.13}WO_3$ with that of the end members of the WO_3-HTB solid solution. The WO_3 and $K_{0.4}WO_3$ half cells were also cycled at a rate of 0.5 C.

Figure 3.15 shows the galvanostatic discharge profiles obtained for $K_{0.13}WO_3$ (solid trace), WO_3 (dashed trace) and $K_{0.4}WO_3$ (dotted trace) at the end of the first discharge when cycled at 0.5 C. All three profiles are very different; however, it is noted that there are some similarities between the profiles obtained for $K_{0.13}$ and $K_{0.4}WO_3$.

It is in the second discharge cycle, however, that the contrast between $K_{0.13}WO_3$ and the end members WO_3 and $K_{0.4}WO_3$ become most apparent. Figure 3.16 shows the galvanostatic charge-discharge profiles obtained for all three systems, clearly indicating the reversibility of intercalation in $K_{0.13}WO_3$ compared to the other two species. More specifically, upon charging, 1.86 Li^+

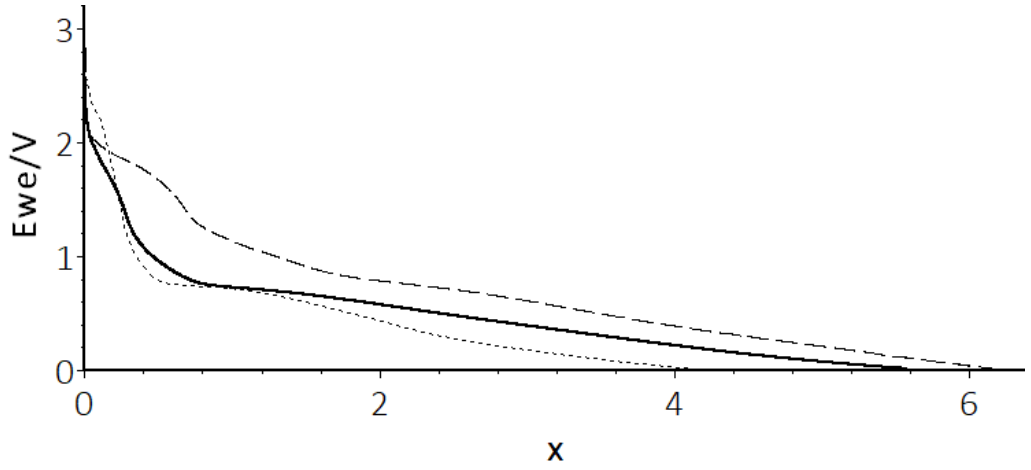

Figure 3.15: Galvanostatic discharge profiles for $K_{0.13}WO_3$ (solid trace), WO_3 (dashed trace) and $K_{0.4}WO_3$ (dotted trace) after the first discharge at 0.5 C. The x-axis denotes the number of Li^+ ions intercalated per formula unit (x).

ions per formula unit are recovered from the electrode, and almost the same number are intercalated during the second discharge. Since there is only one transition metal atom in each formula unit of $K_{0.13}WO_3$, this directly corresponds to a capacity of 1.86 Li^+/TM (189.4 mA h g^{-1}). In comparison, only 0.4 Li^+ ions per formula unit are reversibly intercalated into WO_3 or $K_{0.4}WO_3$. It is also interesting to note that at the end of the first charge, $K_{0.13}WO_3$ and WO_3 retain the same number of Li^+ ions per formula unit in the SEI layer, potentially shedding light on the nature of the SEI layer after Li^+ has been extracted from the active material.

$K_{0.13}WO_3$ also demonstrated good cyclability when cycled to the end of the third consecutive discharge. As shown in Figure 3.17, the SEI layer developed further between the second and third discharge cycles, which is to be expected as lithium is lost to the SEI between cycles; however, the capacity only dropped by 0.16 Li^+/TM (17.8 mA h g^{-1}). Furthermore, the same total number of Li^+ ions per formula unit was reached during each discharge, implying that any Li^+ ions not contributing to the continued evolution of the SEI layer were being reversibly intercalated into the active material. Further testing over a greater number of cycles would be needed to confirm whether the SEI layer continues to grow over time, or whether the capacity fade between the second and third discharge cycles is quickly reduced.

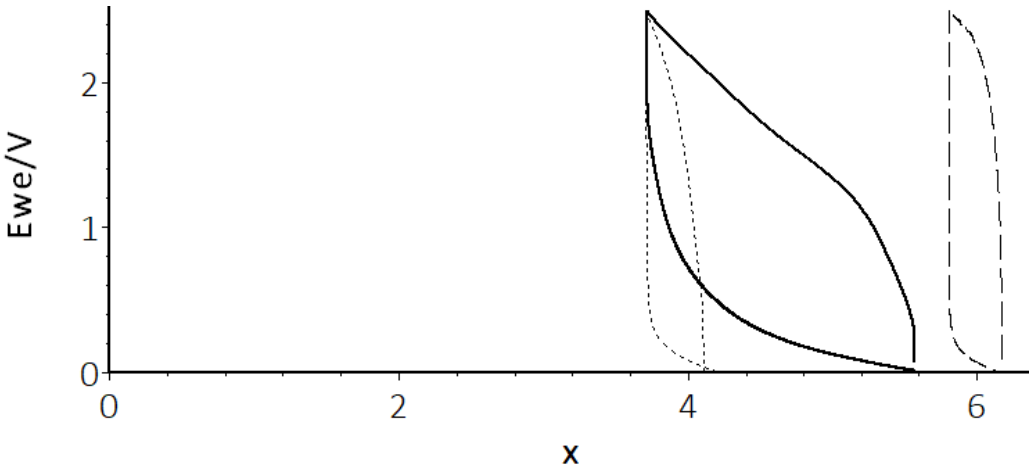

Figure 3.16: Galvanostatic charge-discharge curves for $K_{0.13}WO_3$ (solid trace), WO_3 (dashed trace) and $K_{0.4}WO_3$ (dotted trace) after the second discharge at 0.5 C. The x-axis denotes the number of Li^+ ions intercalated per formula unit (x).

(a)

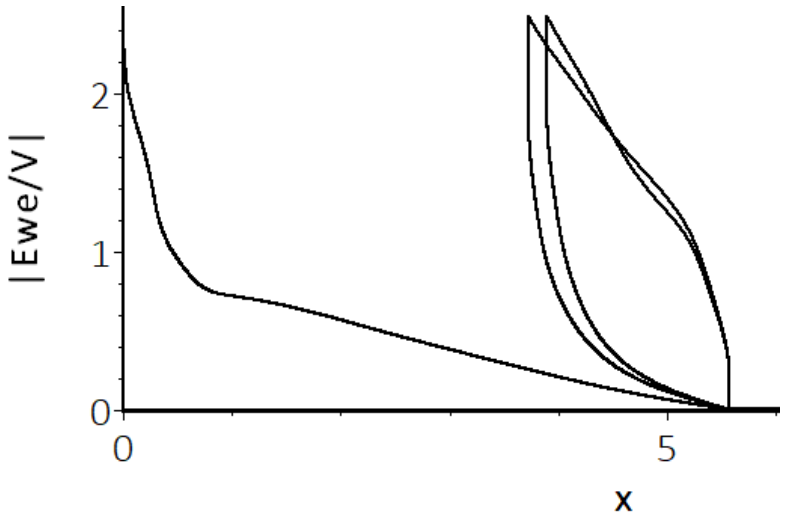

(b)

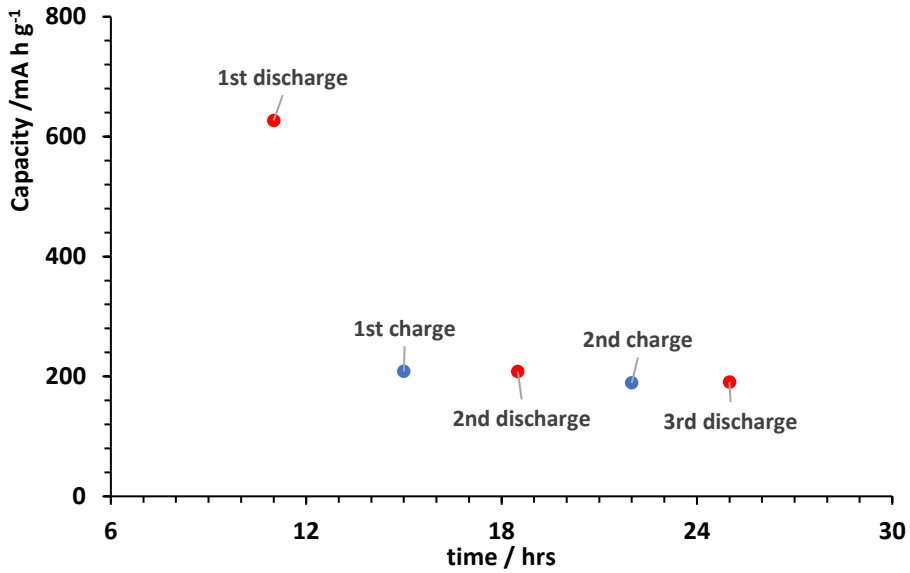

Figure 3.17: (a) Galvanostatic discharge-charge profile for $K_{0.13}WO_3$ to the end of the 3rd discharge at 0.5 C, where the x-axis denotes the number of Li^+ ions intercalated per formula unit, x, and (b) corresponding capacity fade.

3.3.3 Solid-State NMR Studies of $K_{0.13}WO_3$

To assist in determining where the Li^+ ions are being intercalated into the structure during discharge, ^{7}Li MAS and ^{6}Li MAS NMR experiments were conducted. Initially, only ^{7}Li MAS NMR experiments were completed, however, the spectrum obtained only contained a single broad peak from which little structural information could be gained, as shown in Figure 3.18. The asymmetrical lineshape suggests there may be two or more resonances close to 0 ppm, one of which may be due to lithium in the SEI layer and the other due to lithium in the active material. The ^{6}Li MAS NMR spectrum obtained appears to confirm this, showing two distinct peaks at δ = 0 ppm and δ = 2.8 ppm, the latter being of greater intensity.

^{6}Li MAS NMR spectra were obtained for a $K_{0.13}WO_3$ electrode at the end of the first charge cycle. The spectrum obtained is shown in Figure 3.19, in red, with the ^{6}Li MAS spectrum of the fully-lithiated electrode shown in blue. As expected, the spectrum obtained at the end of the first charge cycle shows only one resonance at approximately δ = 0 ppm, corresponding to the lithium contained within the SEI layer. Therefore, the peak at δ = 2.80 ppm in the previous spectrum is the result of the intercalated lithium in the active material, though it does not describe the precise nature of that lithium environment – i.e., whether lithium was intercalated into the channels present in the WO_3 phase, the HTB phase, or both.

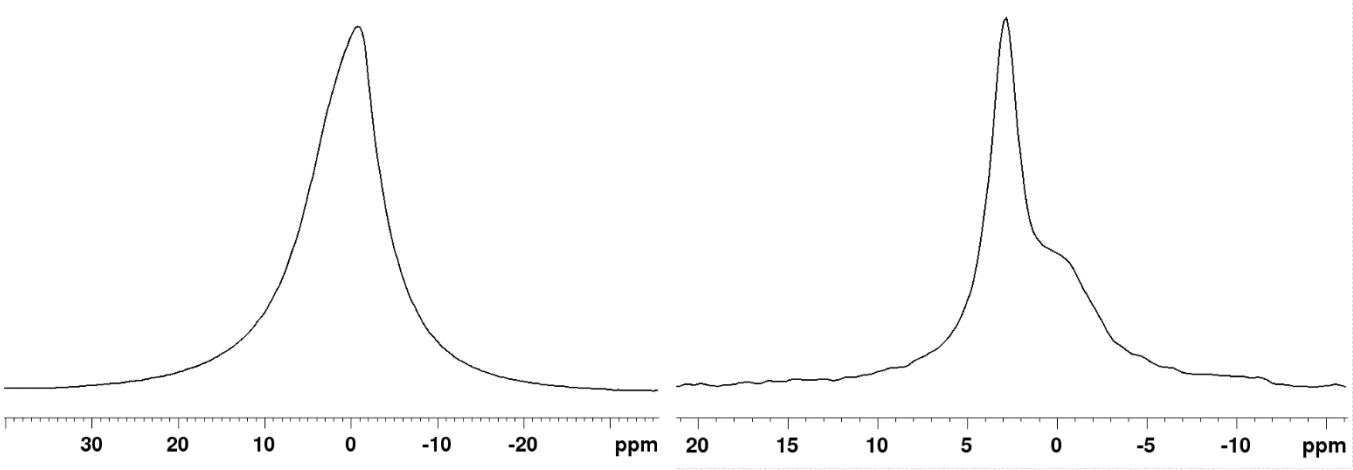

Figure 3.18: ^{7}Li MAS (left) and ^{6}Li MAS NMR (right) spectra of $K_{0.13}WO_3$ after 1st discharge. MAS rate: 10 kHz. Only the central transition is shown, omitting the manifold of spinning sidebands that were present.

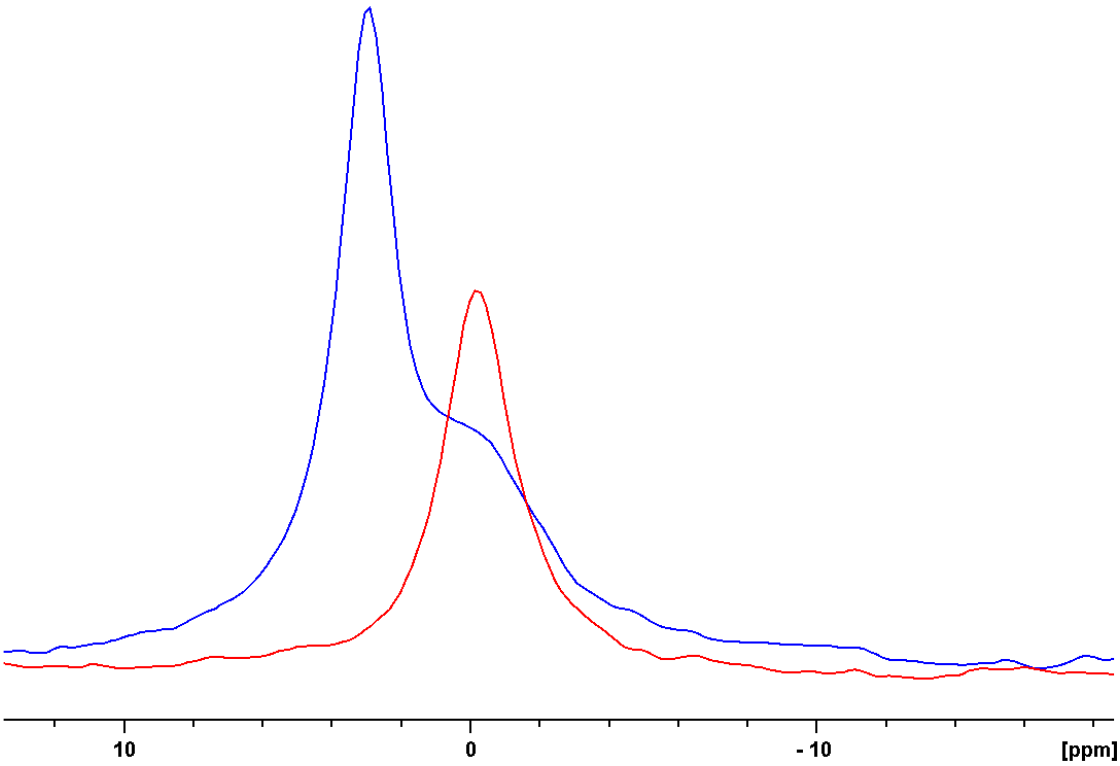

Figure 3.19: ^{6}Li MAS NMR spectra obtained for $K_{0.13}WO_3$ at the end of the 1st discharge (blue trace) and after 1st charge (red trace). MAS rate: 10 kHz.

Subsequently, ^{6}Li MAS NMR experiments were completed on WO_3 and $K_{0.4}WO_3$ electrodes which had been discharged at 0.5 C. The spectra obtained for these samples, at the end of the first discharge, are shown in Figure 3.20. Lithiated $K_{0.4}WO_3$ (top) exhibits a broader peak close to δ = 0 ppm, however, it is not clear whether this broadening is due to multiple overlapped resonances or disordering of the Li environments in this region of the spectrum or not. On the other hand, lithiated WO_3 (bottom) exhibits two distinct peaks, one at approximately δ = 0 ppm and the other at δ = 2.66 ppm. However, it is noted that the peak at δ = 2.66 ppm is not as intense as the peak seen in the ^{6}Li MAS spectrum obtained for $K_{0.13}WO_3$ at δ = 2.80 ppm, which correlates with the reduced capacity for lithiation displayed by WO_3. It is reasonable to conclude, therefore, that lithium intercalates into the WO_3 phase in $K_{0.13}WO_3$. Lithium may also intercalate into the hexagonal phase, which is also present; the NMR data obtained does not exclude this possibility, as the region between the two resonances in the spectrum corresponding to $K_{0.13}WO_3$ is where a contribution from a resonance in the hexagonal phase might be expected.

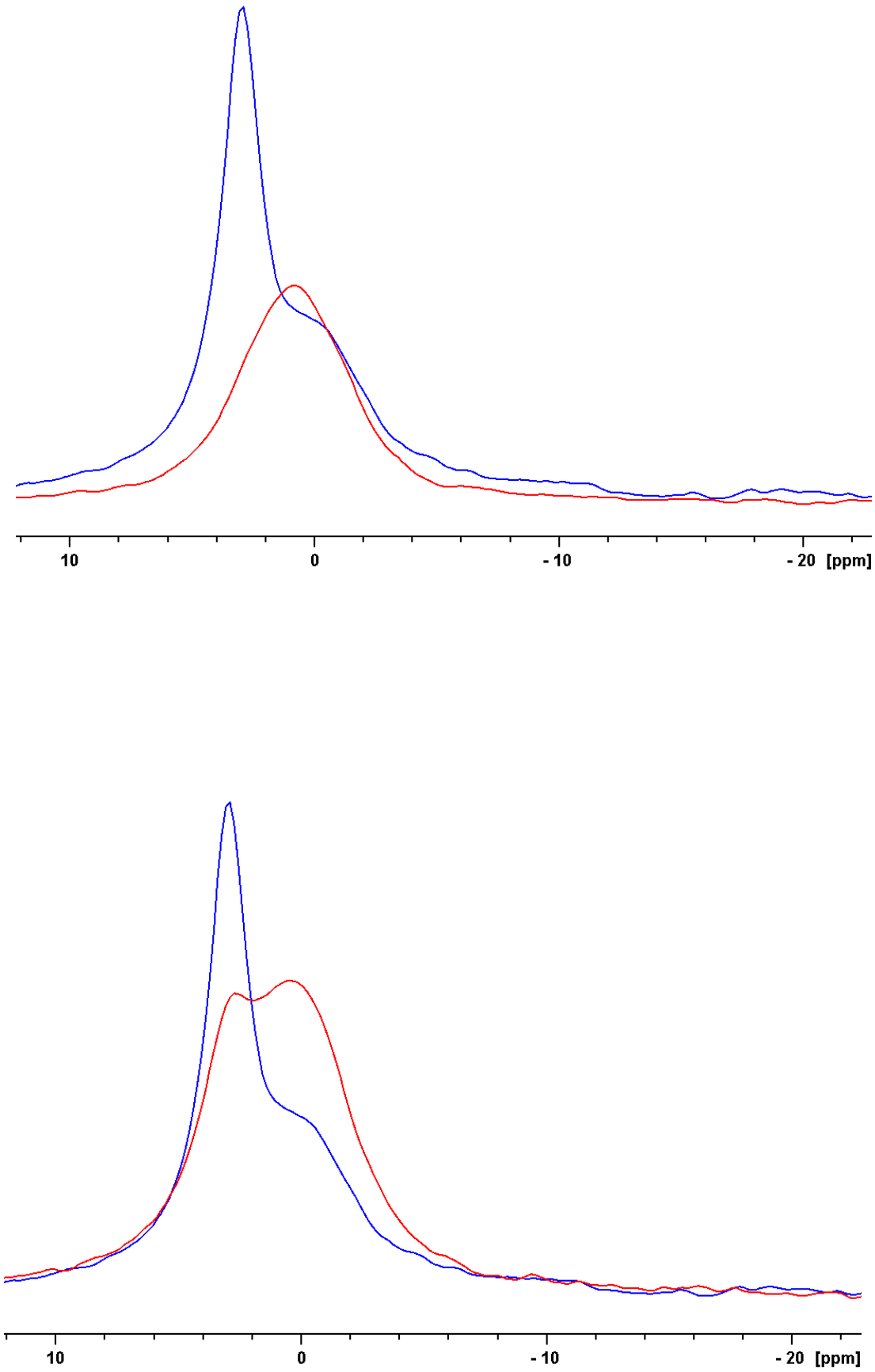

Figure 3.20: ^{6}Li MAS NMR spectra of $K_{0.4}WO_3$ (top, red trace) and WO_3 (bottom, red trace) after the first discharge at 0.5 C. The ^{6}Li MAS NMR spectrum of $K_{0.13}WO_3$ is shown in blue. MAS rate: 10 kHz.

Chapter 4 Conclusions and Future Work

The experimental methods used by Griffith et al. were used to synthesise shear-type $Nb_{16}W_5O_{55}$ and bronze-like $Nb_{6.7}W_{10.3}O_{47}$.[71] PXRD measurements and subsequent Rietveld refinements were successful in confirming the presence of each structure in their respective samples. Samples containing shear-type $Nb_{16}W_5O_{55}$ were also shown to contain similar shear-type structures, likely present as Wadsley defect fringes, whilst the synthesise of $Nb_{6.7}W_{10.3}O_{47}$ proved challenging due to the occasional formation of the $Nb_{18}W_{16}O_{93}$. Galvanostatic measurements were taken for half-cells containing $Nb_{6.7}W_{10.3}O_{47}$ as the active material, which showed similar electrochemical performance to the bronze-like $Nb_{18}W_{16}O_{93}$ structure reported by Griffith et al. [71] However, whilst the capacity of these half cells was good (1.60 Li^+/TM on the third discharge), the capacity was expected to fade over subsequent cycles.

Taking inspiration from the structural motifs which provided these niobium tungsten oxides their excellent performance as anodes, a modified version of the synthetic method outlined by Hussain and Kihlborg in 1976 was used to synthesised K_xWO_3 samples from WO_2, WO_3 and K_2WO_4 in the presence of air.[92] Although optical microscopy and HREM experiments were not undertaken, PXRD experiments and subsequent Rietveld refinements on a sample of K_xWO_3 (x = 0.13) confirmed the presence of a hexagonal phase similar to $K_{0.3}WO_3$, alongside a sizeable phase fraction of WO_3. It is unclear from these Rietveld refinements whether the WO_3 phase was unreacted material or whether it was a contribution from the interlocking phase observed by Hussain and Kihlborg.[92] Although X-ray diffraction experiments typically yield information about the long-range order within a crystal structure, previous experiments on shear-type $Nb_{16}W_5O_{55}$ shows that the presence of Wadsley defect fringes leads to complex diffraction patterns which are challenging to interpret. In fact, $Nb_{16}W_5O_{55}$, discussed in Section 3.1, can be considered an interlocking phase and, likewise, the hexagonal phase present in interlocking $K_{0.13}WO_3$ can be considered a Wadsley defect fringe.

For this reason, it was assumed that the hexagonal and WO_3 phases present were interlocking. Galvanostatic discharge-charge data up to an including the third discharge showed that $K_{0.13}WO_3$ performs exceptionally compared to WO_3 and hexagonal $K_{0.3}WO_4$, demonstrating a capacity of 1.60

Li^+/TM (171.6 mA h g^{-1}) on the third discharge, exceeding that of $Nb_{16}W_5O_{47}$ (~1.5 Li^+/TM) and $Nb_{18}W_{16}O_{93}$ (~1.4 Li^+/TM) reported by Griffith et al. at similar rates of discharge. Alongside its capacity, the galvanostatic measurements taken also demonstrated the reversibility of intercalation in $K_{0.13}WO_3$ compared to WO_3 and $K_{0.3}WO_3$. Solid-state ^{7}Li and ^{6}Li MAS NMR experiments strongly suggest that lithium reversibly intercalates into a WO_3-like environment rather than the hexagonal phase, likely due to the presence of K^+ ions intrinsically accommodated within the latter. However, the galvanostatic measurements and solid-state NMR experiments do not indicate whether $K_{0.13}WO_3$ has an interlocking structure as described by Hussain and Kihlborg, whether it contains larger WO_3 and hexagonal block-like domains side-by-side, or whether it contains WO_3 and hexagonal phases separated by grain boundaries.[92]

Much work remains to be done on the K_xWO_3 series in general. Galvanostatic studies should be carried out at higher rates for $K_{0.13}WO_3$ and then replicated across the series. Further ^{6}Li MAS NMR experiments should be conducted to identify any changes to the lithium environments over successive cycles. In addition, electron microscopy techniques should be employed to verify the surface structure of $K_{0.13}WO_3$ and to identify the presence of an interlocking phase.

References

1 H. Clark and C. Frankland, Dig. United Kingdom Energy Stat., 2018, Chapter 1-Electricity.

2 C. Sevim, Dig. United Kingdom Energy Stat., 2019, Chapter 1-Elecricity.

3 H. Clark and C. Frankland, Dig. United Kingdom Energy Stat. 2018, 2018, July, Chapter 6-Renewable Sources of Energy.

4 S. Dutta, J. Ind. Eng. Chem., 2014, 20, 4, 1148-1156.

5 R. Marom, S. F. Amalraj, N. Leifer, D. Jacob and D. Aurbach, J. Mater. Chem., 2011, 21, 9938–9954.

6 L. Zhang and C. Chen, Prog. Chem., 2018, 1, 2, 182-187

7 N. Armaroli and V. Balzani, Energy Environ. Sci., 2011, 4, 3193–3222.

8 J. B. Goodenough and K.-S. Park, J. Am. Chem. Soc., 2013, 135, 1167–1176.

9 J. B. Goodenough and K.-S. Park, J. Am. Chem. Soc., 2013, 135, 1167–1176.

10 D. B. Hibbert, ed. D. B. Hibbert, Macmillan Education UK, London, 1993, pp. 1–10.

11 M. Winter, B. Barnett and K. Xu, Chem. Rev., 2018, 118, 11433–11456.

12 R. M. Dell and D. A. J. Rand, Understanding Batteries, The Royal Society of Chemistry, 2001.

13 F. R. Gamble, J. H. Osiecki and M. Cais, Sci., 1971, 174, 4008, 493-497.

14 M. S. Whittingham, J. Electrochem. Soc., 1976, 123, 315.

15 M. S. Whittingham, Chem. Rev., 2004, 104, 4271–4301.

16 W. S. Kim and W. Yoon, Electrochim. Acta, 2004, 50, 541–545.

17 K. Mizushima, P. C. Jones, P. J. Wiseman and J. B. Goodenough, Mater. Res. Bull., 1980, 15, 783–789.

18 T. Nagaura and K. Tozawa, Prog. Batter. Sol. Cells, 1990, 9, 209.

19 J. B. Goodenough and Y. Kim, Chem. Mater., 2010, 22, 587–603.

20 D. Lin, Y. Liu and Y. Cui, Nat. Nanotechnol., 2017, 12, 194–206.

21 W. Xu, J. Wang, F. Ding, X. Chen, E. Nasybulin, Y. Zhang and J.-G. Zhang, Energy Environ. Sci., 2014, 7, 513–537.

22 R. Cao, W. Xu, D. Lv, J. Xiao and J.-G. Zhang, Adv. Energy Mater., 2015, 5, 1402273.

23 T. Tao, S. Lu, Y. Fan, W. Lei, S. Huang and Y. Chen, Adv. Mater., 2017, 29, 1700542.

24 C.-F. Lin, Y. Qi, K. Gregorczyk, S. B. Lee and G. W. Rubloff, Acc. Chem. Res., 2018, 51, 97–106.

25 C. Yang, K. Fu, Y. Zhang, E. Hitz and L. Hu, Adv. Mater., 2017, 29, 1701169.

26 Y. Wang, E. Sahadeo, G. Rubloff, C.-F. Lin and S. B. Lee, J. Mater. Sci., 2019, 54, 3671–3693.

27 K. Xu, Chem. Rev., 2004, 104, 4303–4418.

28 K. Hayashi, Y. Nemoto, S. Tobishima and J. Yamaki, Electrochim. Acta, 1999, 44, 2337–2344.

29 T. Kawamura, S. Okada and J. Yamaki, J. Power Sources, 2006, 156, 547–554.

30 C. Sun, J. Liu, Y. Gong, D. P. Wilkinson and J. Zhang, Nano Energy, 2017, 33, 363–386.

31 Y. Zhao and L. L. Daemen, J. Am. Chem. Soc., 2012, 134, 15042–15047.

32 K. Takada, Acta Mater., 2013, 61, 759–770.

33 Y. Inaguma, C. Liquan, M. Itoh, T. Nakamura, T. Uchida, H. Ikuta and M. Wakihara, Solid State Commun., 1993, 86, 689–693.

34 Y. Ren, K. Chen, R. Chen, T. Liu, Y. Zhang and C.-W. Nan, J. Am. Ceram. Soc., 2015, 98, 3603–3623.

35 C. Delmas, A. Nadiri and J. L. Soubeyroux, Solid State Ionics, 1988, 28–30, 419–423.

36 Q. Wang, P. Ping, X. Zhao, G. Chu, J. Sun and C. Chen, J. Power Sources, 2012, 208, 210–224.

37 R. Guo, L. Lu, M. Ouyang and X. Feng, Sci. Rep., 2016, 6, 30248.

38 H. Maleki and J. Howard, J. Power Sources, 2006, 160, 1395–1402.

39 L. Zhang, Y. Ma, X. Cheng, C. Du, T. Guan, Y. Cui, S. Sun, P. Zuo, Y. Gao and G. Yin, J. Power Sources, 2015, 293, 1006–1015.

40 C. Li, H. P. Zhang, L. J. Fu, H. Liu, Y. P. Wu, E. Rahm, R. Holze and H. Q. Wu, Electrochim. Acta, 2006, 51, 3872–3883.

41 H. Yoo, E. Markevich, G. Salitra, D. Sharon and D. Aurbach, Mater. Today, 2014, 17, 110–121.

42 P. Poizot, S. Laruelle, S. Grugeon, L. Dupont and J.-M. Tarascon, Nature, 2000, 407, 496-499..

43 J. Cabana, L. Monconduit, D. Larcher and M. R. Palacín, Adv. Mater., 2010, 22, E170–E192.

44 W. Zhou, J. Zhu, C. Cheng, J. Liu, H. Yang, C. Cong, C. Guan, X. Jia, H. J. Fan, Q. Yan, C. M. Li and T. Yu, Energy Environ. Sci., 2011, 4, 4954–4961.

45 S. Li, A. Li, R. Zhang, Y. He, Y. Zhai and L. Xu, Nano Res., 2014, 7, 1116–1127.

46 A. Vu, Y. Qian and A. Stein, Adv. Energy Mater., 2012, 2, 1056–1085.

47 I.-H. Ko, A. Jin, M. K. Kim, J.-H. Park, H. S. Kim, S.-H. Yu and Y.-E. Sung, J. Alloys Compd., 2020, 817, 152760.

48 S. Goriparti, E. Miele, F. De Angelis, E. Di Fabrizio, R. Proietti Zaccaria and C. Capiglia, J. Power Sources, 2014, 257, 421–443.

49 C. Wu, X. Tong, Y. Ai, D.-S. Liu, P. Yu, J. Wu and Z. M. Wang, Nano-Micro Lett., 2018, 10, 40.

50 B. Wang, B. Luo, X. Li and L. Zhi, Mater. Today, 2012, 15, 544–552.

51 C. Liu, F. Li, L.-P. Ma and H.-M. Cheng, Adv. Mater., 2010, 22, E28–E62.

52 B. A. Boukamp, J. Electrochem. Soc., 1981, 128, 725.

53 C. K. Chan, H. Peng, G. Liu, K. McIlwrath, X. F. Zhang, R. A. Huggins and Y. Cui, Nat. Nanotechnol., 2008, 3, 31–35.

54 Z.-L. Xu, B. Zhang, S. Abouali, M. Akbari Garakani, J. Huang, J.-Q. Huang,

E. Kamali Heidari and J.-K. Kim, J. Mater. Chem. A, 2014, 2, 17944–17951.

55 B. Malaman and J. Steinmetz, J. Less Common Met., 1979, 65, 285–288.

56 P.-Y. Silvert, R. Herrera-Urbina and K. Tekaia-Elhsissen, J. Mater. Chem., 1997, 7, 293–299.

57 C. Marino, A. Darwiche, N. Dupré, H. A. Wilhelm, B. Lestriez, H. Martinez, R. Dedryvère, W. Zhang, F. Ghamouss, D. Lemordant and L. Monconduit, J. Phys. Chem. C, 2013, 117, 19302–19313.

58 S. Flandrois and B. Simon, Carbon N. Y., 1999, 37, 165–180.

59 Y. Nishi, Chem. Rec., 2001, 1, 406–413.

60 Z. Chen, I. Belharouak, Y.-K. Sun and K. Amine, Adv. Funct. Mater., 2013, 23, 959–969.

61 G.-N. Zhu, Y.-G. Wang and Y.-Y. Xia, Energy Environ. Sci., 2012, 5, 6652–6667.

62 C. Ding, Y. Bai, C. Wei and C. Chen, Chinese J. Chem. Phys., 2012, 25, 457–462.

63 V. S. Hernandez, L. M. T. Martinez, G. C. Mather and A. R. West, J. Mater. Chem., 1996, 6, 1533–1536.

64 P. Afanasiev and C. Geantet, Coord. Chem. Rev., 1998, 178–180, 1725–1752.

65 Y. Hao, Q. Lai, D. Liu, Z. Xu and X. Ji, Mater. Chem. Phys., 2005, 94, 382–387.

66 A. S. Prakash, P. Manikandan, K. Ramesha, M. Sathiya, J.-M. Tarascon and A. K. Shukla, Chem. Mater., 2010, 22, 2857–2863.

67 M. F. Oszajca, M. I. Bodnarchuk and M. V Kovalenko, Chem. Mater., 2014, 26, 5422–5432.

68 M. R. Palacin, P. Simon and J. M. Tarascon, Acta Chim. Slov., 2016, 63, 417–423.

69 H. Wu, G. Chan, J. W. Choi, I. Ryu, Y. Yao, M. T. McDowell, S. W. Lee, A. Jackson, Y. Yang, L. Hu and Y. Cui, Nat. Nanotechnol., 2012, 7, 310–315.

70 J. Kasnatscheew, T. Placke, B. Streipert, S. Rothermel, R. Wagner, P.

Meister, I. C. Laskovic and M. Winter, J. Electrochem. Soc., 2017, 164, A2479--A2486.

71 S. Stramare, V. Thangadurai and W. Weppner, Chem. Mater., 2003, 15, 3974–3990.

72 R. Abdul Rani, A. Zoolfakar, A. O'Mullane, M. W. Austin and K. Kalantar-zadeh, J. Mater. Chem. A, 2014, 2, 15683-15703.

73 K. J. Griffith, A. C. Forse, J. M. Griffin and C. P. Grey, J. Am. Chem. Soc., 2016, 138, 8888–8899.

74 K. J. Griffith, K. M. Wiaderek, G. Cibin, L. E. Marbella and C. P. Grey, Nature, 2018, 559, 556–563.

75 R. S. Roth, Prog. Solid State Chem, 1980, 13, 159–192.

76 R. S. Roth and J. L. Waring, J. Res. Natl. Bur. Stand. Sect. A, Phys. Chem., 1966, 70A, 281–303.

77 J. G. Allpress and R. S. Roth, J. Solid State Chem., 1971, 3, 209–216.

78 R. J. Cava, A. Santoro, D. W. Murphy, S. M. Zahurak and R. S. Roth, J. Solid State Chem., 1983, 50, 121–128.

79 M. S. Islam, D. J. Driscoll, C. A. J. Fisher and P. R. Slater, Chem. Mater., 2005, 17, 5085–5092.

80 A. Magnéli, Act Chem. Scand., 1953, 7, 315–324.

81 A. Magnéli, Ark. Kemi, 1949, 1, 213–221.

82 I. . Szilagyi, J. Madarasz, G. Pokol, G. Kiraly, G. Tarkanvi, S. Saukko, J. Mizsei, A. L. Toth, A. Szabo and K. Varga-Josepovits, Chem. Mater., 2008, 20, 4116–4125.

83 V. Hornebec, J. M. Reau and J. Ravez, Solid State Ionics, 2000, 127, 231–240.

84 A. Kuhn, H. Bashir, A. L. Dos Santos, J. L. Acosta and F. Garcia-Alvarado, J. Solid State Chem., 2004, 177, 2366–2372.

85 V. A. Isupov, Ferroelectrics, 1985, 65, 181–199.

86 N. Kumagai, A. Yu and H. Yashiro, Solid State Ionics, 1997, 98, 159–166.

87 K. P. Reis, A. Ramanan and M. S. Whittingham, J. Solid State Chem., 1992, 96, 31–47.

88 J.-D. Guo, K. P. Reis and M. Stanley Whittingham, Solid State Ionics, 1992, 53–56, 305–314.

89 A. Simon and J. Ravez, Comptes Rendus Chim., 2006, 9, 1268–1276.

90 A. B. Haugen, G. H. Olsen, F. Madaro, M. I. Morozov, G. Tutuncu, J. L. Jones, T. Grande and M.-A. Einarsrud, J. Am. Ceram. Soc., 2014, 97, 3818–3825.

91 L. G. Van Uitert, H. J. Levinstein, J. J. Rubin, C. D. Capio, E. F. Dearborn and W. A. Bonner, Mater. Res. Bull., 1968, 3, 47–57.

92 A. Hussain and L. Kihlborg, Acta Crystallogr. Sect. A, 1976, 32, 551–557.

93 West. A, Solid State Chemistry and its Applications, 2014.

94 W. Clegg, X-ray Crystallography, Oxford, 2015.

95 J. Kieffer and J. Wright, Powder Diffr., 2013, 28, S2, S339-S350.

96 M. Hellenbrandt, Crystallogr. Rev., 2004, 10, 17–22.

97 A. H. Toby and R. B. Von Dreele, J. Appl. Crystallogr., 2013, 46, 544–549.

98 M. H. Levitt, Spin Dynamics: Basics of Nuclear Magnetic Resonance, Wiley, 2008.

99 J. Keeler, Understanding NMR Spectroscopy, Wiley, 2010.

100 P. J. Hore, Nuclear Magnetic Resonance, Oxford, 2015.

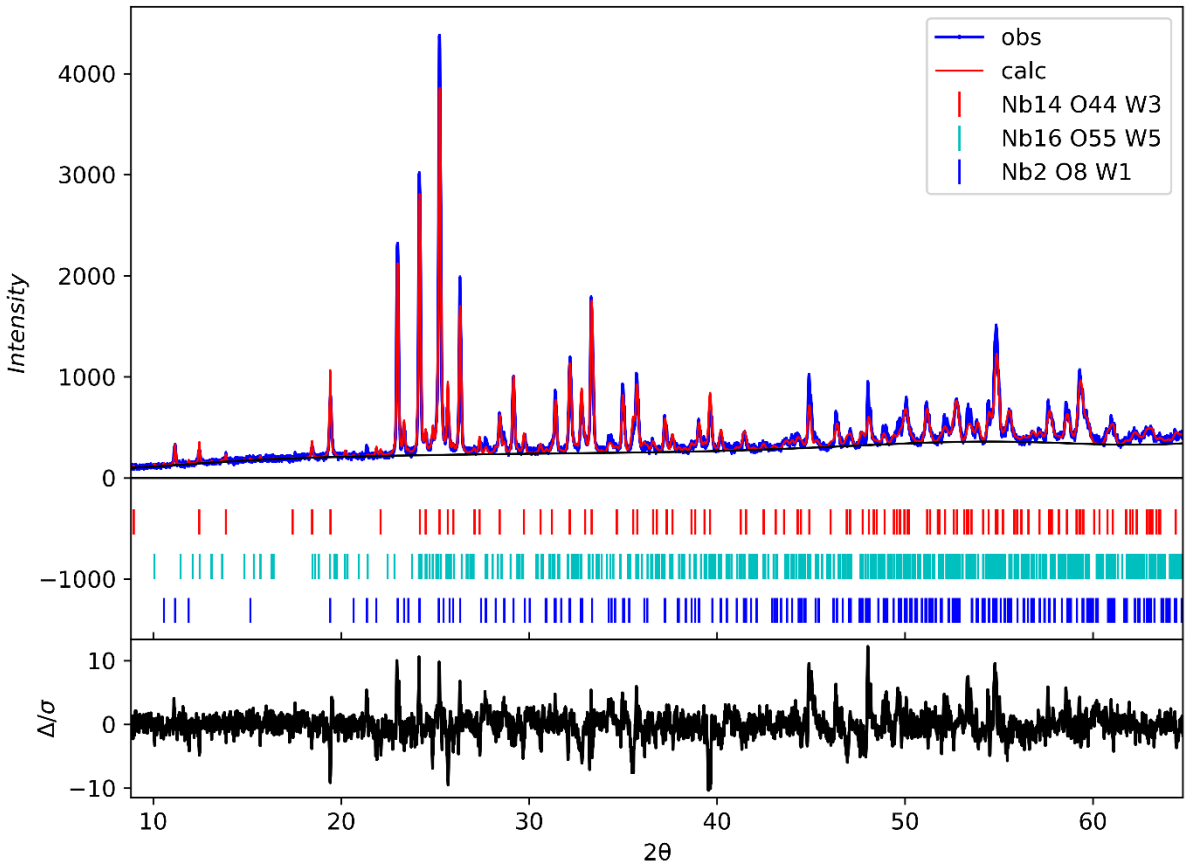

Figure S.1: Rietveld refinement of the PXRD data obtained from the initial sample of $Nb_{16}W_5O_{55}$ after being heated for an additional 4 hours. Phase composition: $Nb_{16}W_5O_{55}$ = 21.7%, $Nb_{14}W_3O_{44}$ = 78.3%; wRp = 14.1%. The difference between the observed and calculated diffraction patterns is shown in black in the lower portion of the plot.

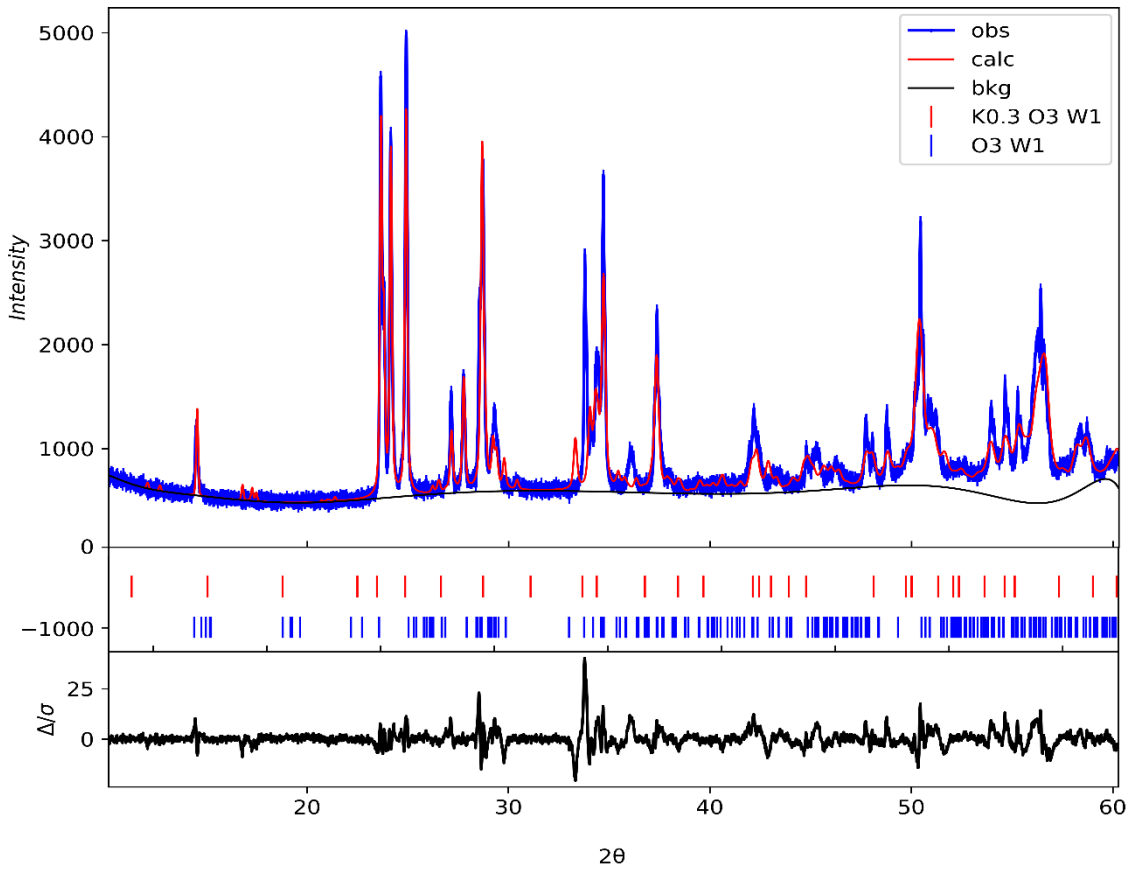

Figure S.2: Rietveld refinement of the PXRD data obtained from a sample of $K_{0.13}WO_3$ synthesised in a box furnace. Phase composition: WO_3 = 66.9%, $K_{0.3}WO_3$ (HTB) = 33.1%; wRp = 15.1%. The difference between the observed and calculated diffraction patterns is shown in black in the lower portion of the plot.